Monthly Notices
of the
ROYAL ASTRONOMICAL SOCIETY

MNRAS **470,** 3775–3805 (2017)
Advance Access publication 2017 May 31

doi:10.1093/mnras/stx1338

VALES I: the molecular gas content in star-forming dusty *H*-ATLAS galaxies up to $z = 0.35$

V. Villanueva,[1⋆] E. Ibar,[1] T. M. Hughes,[1] M. A. Lara-López,[2,3] L. Dunne,[4,5] S. Eales,[5] R. J. Ivison,[6,4] M. Aravena,[7] M. Baes,[8] N. Bourne,[4] P. Cassata,[1] A. Cooray,[9,10] H. Dannerbauer,[11,12] L. J. M. Davies,[13] S. P. Driver,[13] S. Dye,[14] C. Furlanetto,[14,15] R. Herrera-Camus,[16] S. J. Maddox,[4,5] M. J. Michałowski,[4] J. Molina,[17] D. Riechers,[18] A. E. Sansom,[19] M. W. L. Smith,[5] G. Rodighiero,[20] E. Valiante[5] and P. van der Werf[21]

Affiliations are listed at the end of the paper

Accepted 2017 May 26. Received 2017 May 25; in original form 2017 February 13

ABSTRACT

We present an extragalactic survey using observations from the Atacama Large Millimeter/submillimeter Array (ALMA) to characterize galaxy populations up to $z = 0.35$: the Valparaíso ALMA Line Emission Survey (VALES). We use ALMA Band-3 CO(1–0) observations to study the molecular gas content in a sample of 67 dusty normal star-forming galaxies selected from the *Herschel* Astrophysical Terahertz Large Area Survey (*H*-ATLAS). We have spectrally detected 49 galaxies at $>5\sigma$ significance and 12 others are seen at low significance in stacked spectra. CO luminosities are in the range of (0.03–1.31) $\times$ 10^{10} K km s^{-1} pc^2, equivalent to $\log(M_{\rm gas}/{\rm M}_\odot) = 8.9$–$10.9$ assuming an $\alpha_{\rm CO} = 4.6$ (K km s^{-1} pc^2)$^{-1}$, which perfectly complements the parameter space previously explored with local and high-z normal galaxies. We compute the optical to CO size ratio for 21 galaxies resolved by ALMA at $\sim$3.5 arcsec resolution (6.5 kpc), finding that the molecular gas is on average ~ 0.6 times more compact than the stellar component. We obtain a global Schmidt–Kennicutt relation, given by $\log[\Sigma_{\rm SFR}/({\rm M}_\odot\,{\rm yr}^{-1}\,{\rm kpc}^{-2})] = (1.26 \pm 0.02) \times \log[\Sigma_{M_{\rm H2}}/({\rm M}_\odot\,{\rm pc}^{-2})] - (3.6 \pm 0.2)$. We find a significant fraction of galaxies lying at 'intermediate efficiencies' between a long-standing mode of star formation activity and a starburst, specially at $L_{\rm IR} = 10^{11\text{–}12}\,{\rm L}_\odot$. Combining our observations with data taken from the literature, we propose that star formation efficiencies can be parametrized by $\log[{\rm SFR}/M_{\rm H_2}] = 0.19 \times (\log {\rm L_{IR}} - 11.45) - 8.26 - 0.41 \times \arctan[-4.84\,(\log L_{\rm IR} - 11.45)]$. Within the redshift range we explore ($z < 0.35$), we identify a rapid increase of the gas content as a function of redshift.

Key words: ISM: lines and bands – galaxies: high-redshift – galaxies: ISM – infrared: galaxies – submillimetre: galaxies.

1 INTRODUCTION

Understanding the way in which galaxies form and evolve throughout cosmic time is one of the major challenges of extragalactic astrophysics. Recently, theoretical models adopting a Λ cold dark matter (ΛCDM) cosmology have been successful in probing the hierarchical gravitational growth of dark matter haloes, which is then associated to the large-scale structure of the observed baryonic matter (e.g. Spergel et al. 2003, 2007). On smaller scales, however, the physical processes that control galaxy growth have intricate non-linear dependencies that make its explanation far from trivial (e.g. Vogelsberger et al. 2014; Crain et al. 2015; Schaye et al. 2015). One of the key observations used to constrain galaxy formation and evolution models is the behaviour of the cosmic star formation rate (SFR) density. Understanding the cosmic evolution of the interplay between the observed SFR, molecular gas content ($M_{\rm gas}$), global stellar mass content ($M_\star$) and gas-phase metallicity (Z) is a major goal in this field of research. We therefore require a detailed knowledge of the origin and the properties of the gas

⋆ E-mail: vicente.villanueva@postgrado.uv.cl

reservoir that ignites and sustains the star formation activity in galaxies at different epochs.

The accretion of gas into the potential wells of galaxies, either from the inter-galactic medium or via galaxy–galaxy interactions, provides the gas reservoir for ongoing and future star formation (Di Matteo et al. 2007; Bournaud, Elmegreen & Martig 2009; Dekel, Sari & Ceverino 2009). Most stars form in giant molecular clouds (GMCs), in which the majority of the mass is in the form of molecular hydrogen (H_2). The lack of a permanent dipole moment in this molecule means that direct measurements of cold H_2 gas are extremely difficult (e.g. Papadopoulos & Seaquist 1999; Bothwell et al. 2013). Thus, an alternative approach to study the molecular gas content is through observations of carbon monoxide (CO) line emission of low-J transitions (e.g. J = 2–1 or J = 1–0) – the best standard tracer of the total mass in molecular gas ($M_{\rm H_2} = \alpha_{\rm CO} L'_{\rm CO(1-0)}$; e.g. Bolatto, Wolfire & Leroy 2013). Even though this tracer has been historically used as a tracer of the molecular gas mass, the $^{12}C^{16}O$ (J = 1–0) [hereafter CO(1–0)] emission line is optically thick, hence the dynamics of the system becomes critical for converting luminosities into masses (Solomon & Vanden Bout 2005). For instance, in the case of a merger where dynamical instabilities are large and the system is not virialized, Doppler-broadening could affect the line profiles and the emitting regions could be more dispersed throughout the interstellar medium (ISM), thus enhancing the CO emission compared to that from a virialized system of the same mass (Downes & Solomon 1998a). In dense, optically thick virialized GMCs, it is found that $\alpha_{\rm CO} \sim 5\,{\rm M}_\odot\,({\rm K\,km\,s^{-1}\,pc^2})^{-1}$, whereas $\alpha_{\rm CO} \sim 0.8\,{\rm M}_\odot\,({\rm K\,km\,s^{-1}\,pc^2})^{-1}$ in more dynamically disrupted systems, such as in ultra luminous infrared galaxies (ULIRGs; Downes & Solomon 1998b). On the other hand, $\alpha_{\rm CO}$ may be boosted in low-metallicity environments due to a lack of shielding dust that enhances photodissociation of the CO molecule (Wolfire, Hollenbach & McKee 2010; Narayanan et al. 2012). For instance, Narayanan et al. (2012) find a parametrization of $\alpha_{\rm CO}$ in terms of gas metallicity, where $\alpha_{\rm CO} \propto Z^{-0.65}$ (mixing both low- and high-z galaxies), similar to that found by Feldmann, Hernandez & Gnedin (2012). A higher redshifts, a flatter slope has been suggested (Genzel et al. 2012).

Recent observations taken with the *Herschel Space Observatory*[1] (Pilbratt et al. 2010) of local star-forming galaxies (SFGs) suggest the existence of at least two different mechanisms triggering the star formation. Taking into account the $L_{\rm FIR}/M_{\rm H_2}$ ratio (where $L_{\rm FIR}$ is the far-IR luminosity) as a tracer of the star formation efficiency, Graciá-Carpio et al. (2011) find an unusual point at $\sim 80\,{\rm L}_\odot\,{\rm M}_\odot^{-1}$ at which average properties of the neutral and ionized gas change significantly, this observation is broadly consistent with a scenario of a highly compressed and more efficient mode of star formation that creates higher ionization parameters that cause the gas to manifest in low line to continuum ratios. This value is similar to the one at which Genzel et al. (2010) and Daddi et al. (2010b) claim a transition to a more efficient star formation mode, above the so-called 'main-sequence' for SFGs (e.g. Elbaz et al. 2011). The different mechanisms controlling the star formation activity are thought to be the product of dynamical instabilities, where higher efficiencies are seen in more compact and dynamically disrupted systems, such as in ultra luminous. Over the last few years, significant efforts have been made to characterize the star formation activity of normal and starburst galaxies at low-z (e.g. Howell et al. 2010; Saintonge et al. 2011; Bauermeister et al. 2013; Bothwell et al. 2014). The construction of large samples of galaxies with direct molecular gas detections (via CO emission) has remained a challenge. Beyond the local Universe, CO detections are limited to the most massive/luminous yet rare galaxies. For example, Braun et al. (2011) report detections of the CO(J = 1–0) transition for 11 ULIRGs with an average redshift of $z = 0.38$. For these ULIRGs, the molecular gas mass as a function of look-back time demonstrates a dramatic rise by almost an order of magnitude from the current epoch out to 5 Gyr ago. In addition, Combes et al. (2011) presented 18 detected ULIRGs at $z \sim 0.2$–0.6 for CO(1–0), CO(2–1) and CO(3–2) with an average CO luminosity of $L'_{\rm CO(1-0)} = 2 \times 10^{10}$ K km s^{-1} pc^2, finding that the amount of gas available for a galaxy quickly increases as a function of redshift. Moreover, Magdis et al. (2014) presented the properties of 17 *Herschel*-selected ULIRGs ($L_{\rm IR} > 10^{11.5}\,{\rm L}_\odot$) at $z = 0.2$–0.8, showing that the previously observed evolution of ULIRGs at those redshifts is already taking place by $z \sim 0.3$. Nevertheless, the observation of 'normal' galaxies at these redshifts (and beyond) has so far been, at least, restricted.

The advent of the Atacama Large Millimeter/submillimeter Array (ALMA) opens up the possibility to explore the still unrevealed nature of the 'normal' SFGs at low-/high-z redshift. In this work, we exploit the *Herschel* Astrophysical Terahertz Large Area Survey (*H*-ATLAS;[2] Eales et al. 2010) and the state-of-the-art capabilities of ALMA to characterize the CO(1–0) line emission ($\nu_{\rm rest} = 115.271$ GHz) of 'normal' star-forming and mildly starburst galaxies up to $z = 0.35$. This paper is organized as follows. Section 2 explains the sample selection, observing strategy and data reduction. In Section 3, we present the main results and the implications of these new ALMA observations to the global context of galaxy evolution. Our conclusion is summarized in Section 4. Throughout this work, we assume a ΛCDM cosmology adopting the values $H_0 = 70.0$ km s^{-1} Mpc^{-1}, $\Omega_{\rm M} = 0.3$ and $\Omega_\Lambda = 0.7$ for the calculation of luminosity distances and physical scales.[3]

2 OBSERVATIONS

2.1 *H*-ATLAS sample

The galaxies presented in this paper have been selected from the equatorial fields of the *H*-ATLAS survey (∼160 deg^2; Valiante et al. 2016) and observed during ALMA Cycle-1 and Cycle-2 (programmes 2012.1.01080.S and 2013.1.00530.S; P.I. E. Ibar). All galaxies have a $>3\sigma$ detection with both the photoconductor array camera and spectrometer (PACS) at 160 μm and the spectral and photometric imaging receiver (SPIRE) at 250 μm, i.e. they are detected near the peak of the spectral energy distribution (SED) of a normal and local SFG. All galaxies have been unambiguously identified in the Sloan Digital Sky Survey (SDSS; Adelman-McCarthy et al. 2008) presenting a significant probability for association (RELIABILITY $R > 0.8$; Smith et al. 2011; Bourne et al. 2016). The optical counterparts to the *Herschel*-detected galaxies all have high-quality spectra from the Galaxy and Mass Assembly survey (GAMA;[4] Z_QUAL ≥ 3; Liske et al. 2015; Driver et al. 2016).

[1] *Herschel* is an ESA space observatory with science instruments provided by European-led Principal Investigator consortia with an important participation from NASA.

[2] http://www.h-atlas.org/

[3] We use Ned Wright's online calculator http://www.astro.ucla.edu/~wright/CosmoCalc.html.

[4] http://www.gama-survey.org/

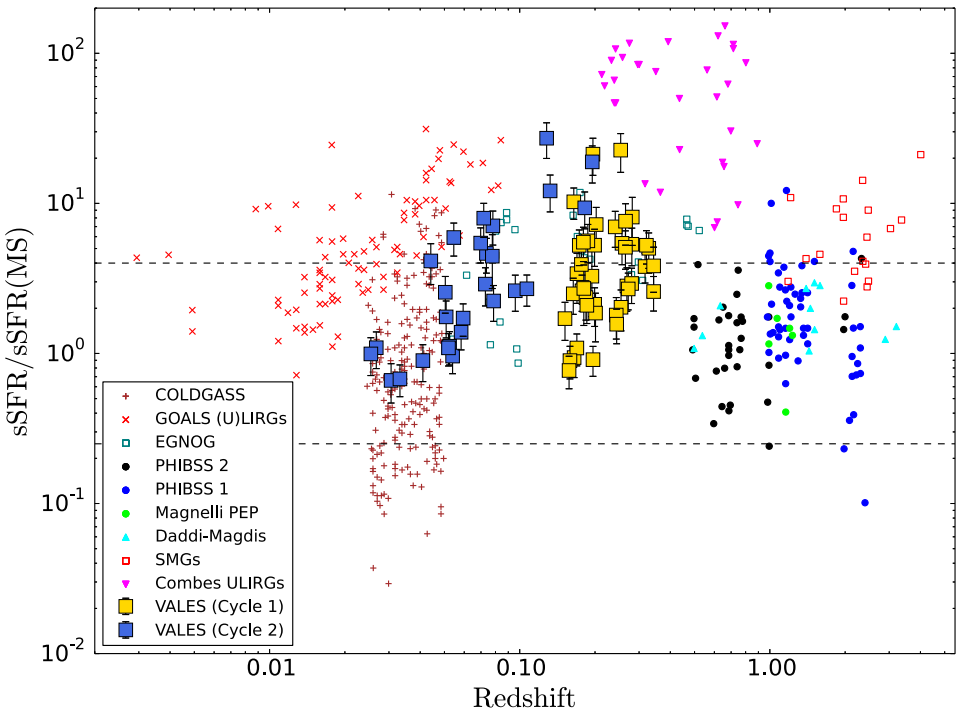

Figure 1. The figure shows the specific SFR (sSFR, defined as sSFR = SFR/$M_\star$), normalized to the one estimated for the 'main sequence' (Elbaz et al. 2011; Whitaker et al. 2012) as a function of redshift for different samples of galaxies detected in CO. We use the parametrization of the 'main sequence' made by Genzel et al. (2015) as $\log[\mathrm{sSFR(MS}, z, M_\star)] = -1.12 + 1.14z - 0.19z^2 - (0.3 + 0.13z) \times (\log M_\star - 10.5)\,\mathrm{Gyr}^{-1}$, where dashed black lines denote 0.6 dex off this equation for SFGs. Our data are presented in filled squares with error bars taken from our ALMA Cycle-1 (yellow) and Cycle-2 (royal blue) campaigns. We estimate the SFR using L_{IR}(8–1000 μm) extracted from the *H*-ATLAS data, stellar masses using MAGPHYS fits (see Section 2.4.3) – both using the same IMF, and redshifts taken from the GAMA survey. Dark red crosses are nearby galaxies (Saintonge et al. 2011), red crosses are (U)LIRGs (Howell et al. 2010), light blue unfilled squares are $z = 0.05$–0.5 normal galaxies (Bauermeister et al. 2013), pink inverted triangles are ULIRGs at intermediate redshifts (Combes et al. 2011, 2013), blue dots are 'main sequence' galaxies at $z = 1$–1.5 and 2–2.5 (Tacconi et al. 2010, 2013), black dots are 'main sequence' galaxies at $z = 0.5$–1 and $z \sim 2$ (Combes & the PHIBSS collaboration 2016), light blue triangles are 'main sequence' galaxies at high-z (Magnelli et al. 2012), light green dots are 'main sequence' galaxies at $z = 0.5$–3.2 (Daddi et al. 2010a; Magdis et al. 2012) and red unfilled squares are submilimetre galaxies at $z = 1.2$–3.4 (Greve et al. 2005; Tacconi et al. 2006, 2008; Bothwell et al. 2013). Figure adapted from Genzel et al. (2015).

Slightly different selection criteria were used in each cycle to construct the list of ALMA targets. In Cycle-1, we selected a representative sample of 41 galaxies with the following criteria: $0.15 < z < 0.35$ [the upper threshold in redshift corresponds to the limits at which the CO(1–0) line moves out of frequency range covered by Band-3 of ALMA]; $S_{160\,\mu\mathrm{m}} > 100$ mJy; SDSS sizes $\mathrm{ISOA} < 10.0$ arcsec; and a reduced $\chi^2 < 1.5$ when fitting the far-IR/submm SED using a modified blackbody (following a similar approach as in Ibar et al. 2013). On the other hand, in Cycle-2 we targeted 27 galaxies that have previous *Herschel* PACS [C II] spectroscopy as shown by Ibar et al. (2015) and so added the following criteria: $0.02 < z < 0.2$ (the threshold is defined by the point where the [C II] is redshifted to the edge of the PACS spectrometer); $S_{160\,\mu\mathrm{m}} > 150$ mJy; Petrosian SDSS radii smaller than 15.0 arcsec; sources do not have $>3\sigma$ PACS 160 μm detections within 2 arcmin (to ensure reliable on–off sky subtraction).

Combining Cycle-1 and Cycle-2 observations, we construct one of the largest samples of CO(1 − 0) detected galaxies at $0.02 < z < 0.35$ (see Fig. 1). We highlight that some of the main advantages of our sample over previous studies of far-IR-selected galaxies are as follows: (1) we cover fainter $L_{8-1000\,\mu\mathrm{m}} \approx 10^{10-12}\,\mathrm{L}_\odot$ and less massive $M_{\mathrm{dust}} \approx 1.5 \times 10^{7-8}\,\mathrm{M}_\odot$ ranges than *IRAS*-selected samples, i.e. our samples are not significantly biased towards powerful ULIRGs that potentially have complex merger morphologies as those described by Braun et al. (2011) and Combes et al. (2011); (2) the sample selection dominated by the 160 and 250 μm photometry gives relatively low dust temperature estimates ($25 < T_{\mathrm{dust}}/\mathrm{K} < 60$) and reduces (but not entirely) the well-known bias towards high dust temperatures evidenced in 60 μm-selected *IRAS* samples (see discussion by Gao & Solomon 2004; Kennicutt et al. 2009); (3) the wealth of ancillary data already available for all the sources (Bourne et al. 2016; Driver et al. 2016) and (4) the redshift range puts galaxies far enough so galaxies can be imaged with a single ALMA pointing in Band-3 – it does not require large mosaicking (using the Atacama Compact Array) campaigns as in more local galaxy samples. These reasons enable us to address our science goals using a much simpler but wider parameter space for the diagnostics of interest (see Fig. 1).

2.2 Observational strategy

ALMA Cycle-1 observations were taken in Band-3 between December 2013 and March 2014 (see Table 1), spending approximately 3–9 min on-source in each source. Scheduling blocks (SBs) were designed to detect the CO(1–0) emission line down to a root mean square (rms) of 1.5 mJy beam^{-1} at 50 km s^{-1} channel width and at ∼3–4 arcsec resolution (the most compact configuration). On the other hand, Cycle-2 observations were taken in Band-3 on 2015 January and SBs were designed to observe the CO(1–0) emission line but down to 2 mJy beam^{-1} at 30 km s^{-1}. Even though ALMA

Table 1. The table shows the way in which our targets were observed during the Cycle-1 and Cycle-2 campaigns.

Project ID	Target names	Observation date	Flux Calibrator	Bandpass Calibrator	Phase Calibrator	PWV [mm]	Number of Antennas
2012.1.01080.S	HATLASJ090633.6+001526, HATLASJ090223.9−001639, HATLASJ091157.2+014453, HATLASJ091420.0+000509, HATLASJ090120.7+020223, HATLASJ085616.0+005237, HATLASJ085957.9+015632, HATLASJ085750.1+012807, HATLASJ091956.9+013852, HATLASJ092232.2+002708, HATLASJ085623.6+001352, HATLASJ085828.4+012211	2014 January 1	Calisto	J0522–3627	J0811+0146	4.217	27
	HATLASJ113858.4−001630, HATLASJ121206.2−013425, HATLASJ114343.9+000203, HATLASJ121141.8−015730, HATLASJ114540.7+002553, HATLASJ114625.0−014511, HATLASJ121427.3+005819, HATLASJ113740.6−010454, HATLASJ121908.7−010159, HATLASJ114702.7+001207, HATLASJ115141.3−004240, HATLASJ121446.4−011155, HATLASJ121253.5−002203, HATLASJ115317.4−010123, HATLASJ115039.5−010640	2013 December 27, ——— 2013 December 29	Mars	J1229+0203	J1229+0203	6.084 ——— 5.757	26
	HATLASJ142517.1+010546, HATLASJ141008.0+005107, HATLASJ142057.9+015233, HATLASJ144218.7+003615, HATLASJ141925.3−011129, HATLASJ141522.0+004413, HATLASJ141908.5+011313, HATLASJ144515.0+003907, HATLASJ140649.0−005646, HATLASJ142208.8+005428, HATLASJ140912.3−013454, HATLASJ144129.5−000901, HATLASJ144116.2+002723	2014 March 9	Ceres, Titan	J1337–1257	J1410+0203	2.223	25
2013.1.00530.S	HATLASJ085356.4+001255, HATLASJ085828.6+003813, HATLASJ085340.7+013348, HATLASJ090005.0+000446, HATLASJ085405.9+011130, HATLASJ085112.9+010342, HATLASJ083745.1−005141, HATLASJ090949.6+014847, HATLASJ090532.6+020222, HATLASJ085346.4+001252, HATLASJ083601.5+002617, HATLASJ084428.4+020350, HATLASJ091205.8+002655		J0750+125	J0750+1231	J0909+0121	2.223	40
	HATLASJ084139.6+015346, HATLASJ084350.8+005534, HATLASJ084305.1+010855, HATLASJ085450.2+021208, HATLASJ083831.8+000044, HATLASJ085111.4+013006, HATLASJ084428.4+020659, HATLASJ084907.1−005138, HATLASJ085234.3+013419, HATLASJ085748.0+004641	2015 January 24	J0750+125	J0739+0137	J0901–0037	5.463	40
	HATLASJ084217.9+021223, HATLASJ085836.0+013149, HATLASJ084630.9+005055, HATLASJ090750.0+010141		Ganymede	J0909+0121	J0901–0037	5.553	39

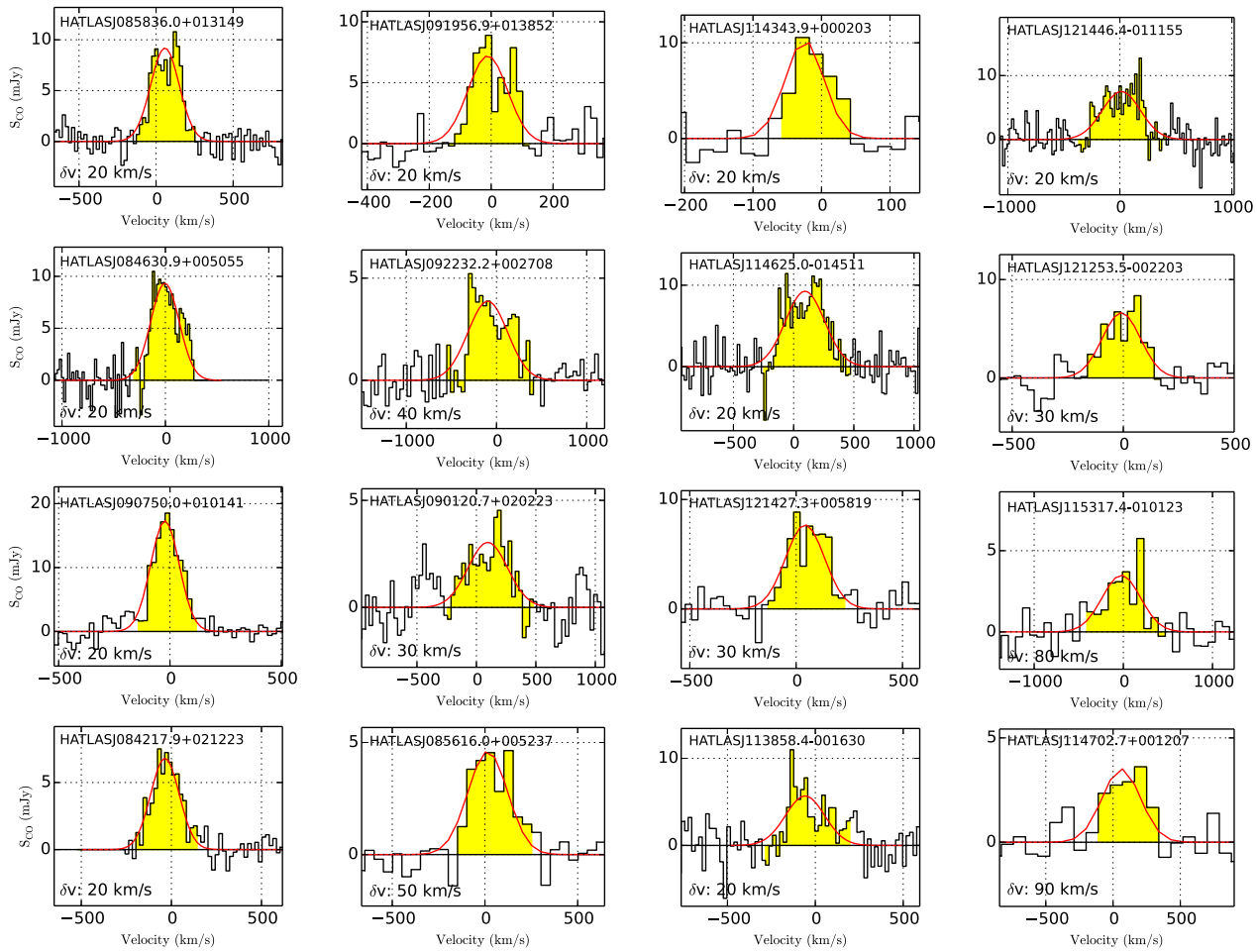

Figure 2. The observed CO(1–0) spectra for spectrally detected galaxies centred on spectroscopic redshifts taken from GAMA. The emission is spectrally binned (δ_v) differently in order to maximize the number of channels with signal above a 5.0σ significance. The yellow colour indicates the spectral range we have used to derive velocity-integrated flux densities. The red lines show best-fitting single Gaussian profiles to the spectra (see Table 2).

is not specifically designed as a 'survey-like' telescope, we setup our experiment to minimize the number of spectral tunings needed to observe all sources independently. We make use of the fact that our targets come from three equatorial *H*-ATLAS/GAMA fields that are $\sim$4 $\times$ 14 deg^2 size, providing large numbers of galaxies at similar redshifts. We modified the 'by-default' approach provided by the ALMA observing tool by setting source redshifts to zero, but fixing the spectral windows (SPWs) manually in order to cover the widest possible spectral range, i.e. redshift range. We optimized the central frequency position of the SPWs (over $\sim$7.5 GHz) to maximize the number of sources with the CO(1–0) line redshifted into the ranges covered by our SPWs. This observing strategy allowed us to spectrally resolve the CO(1–0) emission in 49 galaxies (see Fig. 2; $\sim$70 per cent of the whole sample), while in 12 others we see low signal to noise emission in collapsed spectra (moment−0).

2.3 Data reduction

A summary of all ALMA observations are shown in Table 1. To process all observations in a standardized way, we developed a common pipeline within the on Astronomy Software Applications[5] (CASA version 4.4.0). Based on the standard pipeline for data processing, we designed our own structured pipeline for calibration, concatenation and imaging. The structure was designed in modules, taking into account the vast amount of data and high flexibility at the time to flag corrupted data. When a science goal has more than one observation, we re-calibrate the phase calibrator to an average flux density (usually variations are seen at $\lesssim$15 per cent) and bootstrap this scaling to the targets before concatenating the observations. The bandpass, flux and phase calibrators for each data set can be seen in Table 1.

In the first instance, imaging was performed using the task CLEAN at different spectral resolutions (from 20 to 100 km s^{-1} in steps of 10 km s^{-1}). We sought the resolution that provided the highest number of non-cleaned point-like detections >5.0σ within the data cube (R.A.–Dec.–ν) near the expected source position. If the source was undetected, then we created the cube at 100 km s^{-1} channel width. After choosing the best resolution, we ran task CLEAN again but this time applying a primary beam correction, manually cleaning the CO line emission down to a threshold of 3.0σ, and choosing an

[5] http://casa.nrao.edu/index.shtml

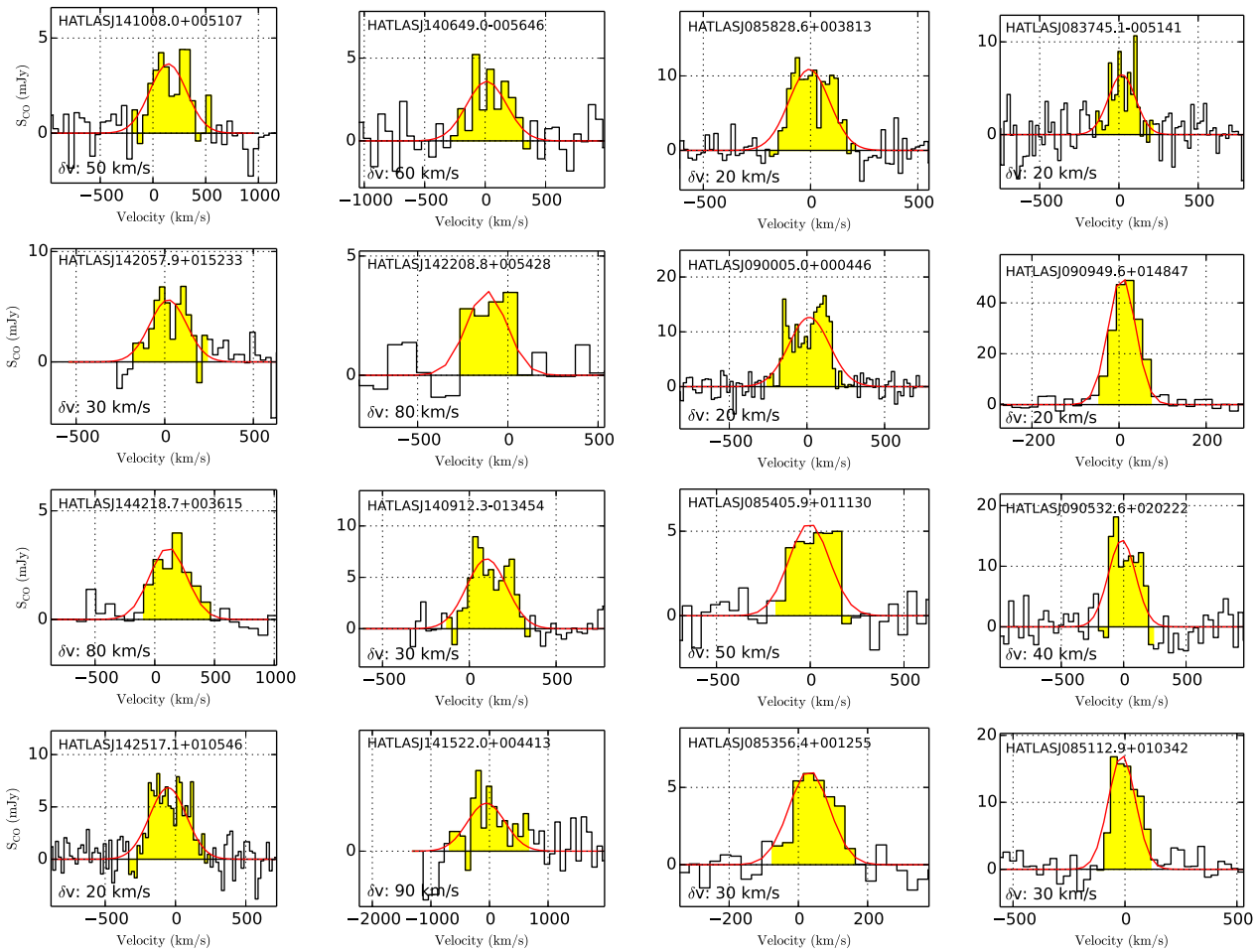

Figure 2 *continued*

image size of 256 × 256 pixels with roughly 5 pixels (semimajor axis) per synthesized beam full width at half-maximum (FWHM). We used the optically derived spectroscopic redshifts ($z_{\rm spec}$) of each source in a barycentric velocity reference frame. The final cubes were created using natural weighting, resulting in image cubes with typical synthesized beams of 3–4 arcsec. The physical sizes for each source, i.e. the deconvolved major-axes (in kpc) are given in Table 2.

2.4 Source properties

2.4.1 CO emission

We get an average rms level of 1.6 mJy beam^{-1} (at 50 km s^{-1}) for both Cycle-1 and Cycle-2. We identify 49 galaxies (out of 67) with a $>5\sigma$ peak line detection in at least one spectral channel (from 10 to 100 km s^{-1} in all binned). For the 49 spectrally detected galaxies, we determine the central frequency ($\nu_{\rm obs}$) of the CO emission line by using a single Gaussian fit to the spectra. We found that central frequencies are in agreement and within the scatter of the expected GAMA's optical redshifts (see column $\nu_{\rm obs}$ in Table 2). The fitted FWHM of the CO line in our sample covers a range of 67–805 km s^{-1}. All the spectra with spectrally resolved CO signal are displayed in Fig. 2, whereas non-detections are summarized in Table 2.

The velocity-integrated CO flux densities ($S_{\rm CO}\Delta v$ in units of Jy km s^{-1}) were obtained by collapsing the data cubes between ±1 × FWHM centred on the line (see yellow range shown in Fig. 2). The 2D intensity map is then fitted with a 2D Gaussian for all detected sources using the task GAUSSFIT within CASA. Errors in these measurements are taken directory from GAUSSFIT's outputs. In seven cases the CO emission is not well fitted by a 2D Gaussian, so we have used an irregular aperture covering the whole extension of the emission. Errors for those aperture measurements come from the standard deviation of fluxes measured in random sky regions around the source. We find measurements in the range of 2.2–20.8 Jy km s^{-1}, with an average value of 6.9 ± 0.2 Jy km s^{-1}. We get 21 galaxies which are spatially resolved in CO, based on a fitted semimajor axis $\sqrt{2}$ times larger than the major axis of the synthesized beam.

For non-detections, we collapsed the cubes (moment 0 maps) between ±250 km s^{-1} centred at the expected observed frequency – a range consistent with the average line width we derive for the whole sample (251.6 ± 38.3 km s^{-1}). In these stacked spectra, 12 other galaxies show emission (ensuring a corrected optical and redshift association). We provide these measurements in Table 2. In these collapsed maps, the rms values range between 0.04 and 5.35 Jy km s^{-1} (at 100 km s^{-1} channel width) with an average of 1.64 Jy km s^{-1}.

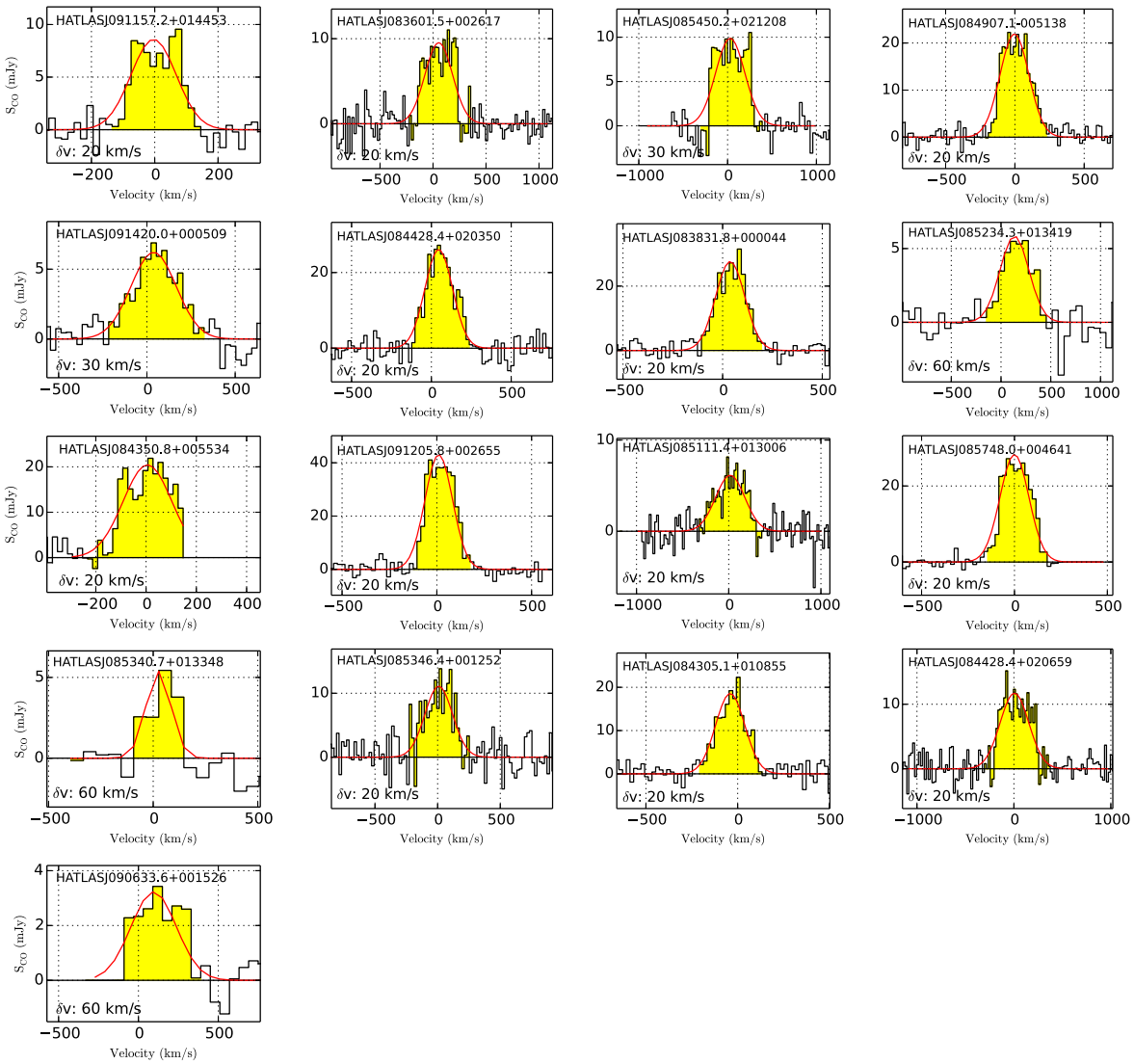

Figure 2 *continued*

Some spectra show double line profiles providing valuable dynamical information. Our kinematic results will be published by Molina et al. (in preparation). We stress, however, that our single Gaussian profiles shown in Fig. 2 are to define the spectral range used to collapse the cubes, from which we obtain the intensity maps to extract the velocity-integrated flux densities. We look at how much the velocity-integrated flux densities could change if we use double Gaussian profiles to fit the emission lines (in 16 spectra). Collapsing the cubes between the lower and the upper FWHM bound limits (of both Gaussians), and comparing these to those obtained from a single Gaussian fit, we obtain that fluxes decrease by a ∼5 per cent (on average), although with a large scatter (∼30 per cent). We decide to stick to the single Gaussian fit to estimate the FWHM to collapse the cubes.

2.4.2 *IR emission*

For each galaxy, we measure the IR luminosity by fitting the rest-frame SED constructed with photometry from *IRAS*, Wide-field Infrared Survey Explorer (WISE), and *Herschel* PACS and SPIRE instruments, using a modified blackbody that is forced to follow a power law at the high-frequency end of the spectrum. The fit constraints the dust temperature ($T_{\rm d}$), the dust emissivity index (β), the mid-IR slope ($\alpha_{\rm mid\text{-}IR}$) and the normalization. Then we integrate the flux of the best-fitting SED between 8 and 1000 μm to obtain the total IR luminosity (Ibar et al. 2013, 2015), i.e.

$$L_{\rm IR}(8\text{–}1000\,\mu{\rm m}) = 4\pi\, D_{\rm L}^2(z) \int_{\nu_1}^{\nu_2} S_\nu \,{\rm d}\nu. \quad (1)$$

The uncertainties on the IR luminosity are obtained by randomly varying the broad-band photometry within the observational uncertainties in a Monte Carlo simulation (100 times). Our results are listed in Table 2.

We estimate the SFR following SFR ($\rm M_\odot\,yr^{-1}$) $= 10^{-10} \times L_{\rm IR}$ assuming a Chabrier (2003) initial mass function (IMF), where $L_{\rm IR}$ is in units of $\rm L_\odot$ (Kennicutt 1998), and we assume a 1.72 factor to convert from a Salpeter to a Chabrier IMF.

Table 2. Observed CO(1–0) line parameters. The z_{spec} and L_{IR} are the optical redshift and total IR luminosity (8–1000 μm). The ν_{obs} is the observed frequency of the line. The v_{obs} and v_{FWHM} are the velocity where the line is centred (with respect to the GAMA redshift) and the FWHM computed by a single Gaussian fit (see Fig. 2). $S_{CO}\Delta v$ is the velocity-integrated flux density from the data cubes collapsed between $v_{obs} - v_{FWHM}$ and $v_{obs} + v_{FWHM}$. L'_{CO} is the CO(1–0) line luminosity using equation (2). M_{H_2} is the mass of the molecular gas using the morphological criteria from Section 2.4.4. R_{FWHM} is the size of the deconvolved semimajor axis of the sources that can be spatially resolved by ALMA (see Section 2.3). SFE is calculated as SFR/M_{H_2}. Σ_{gas} and Σ_{SFR} are the surface density of the gas (molecular and atomic) and SFR, respectively. τ_{gas} is the gas consumption time-scale, and is calculated as SFE^{-1}. Fluxes for sources that are not spectrally detected in CO are calculated collapsing the data cubes between $v_{obs} - \langle v_{FWHM}\rangle$ and $v_{obs} + \langle v_{FWHM}\rangle$, where $\langle v_{FWHM}\rangle = 250$ km s^{-1}, the average FWHM found for the whole sample (see Section 2.4).

GAMA ID	Source	RA (J2000)	Dec. (J2000)	z_{spec}	$\log[L_{IR}/L_\odot]$	SFR [$M_\odot$ yr^{-1}]	$\log[M_\star/M_\odot]$	sSFR (Gyr^{-1})	ν_{obs} (GHz)	v_{obs} (km s^{-1})	v_{FWHM} (km s^{-1})	$S_{CO}\Delta v$ (Jy km s^{-1})	$L'_{CO}/10^{10}$ (K km s^{-1} pc^2)	$\log[M_{H2}/M_\odot]$	R_{FWHM} (kpc)	SFE (Gyr^{-1})	Σ_{gas} ($\log M_\odot$ pc^{-2})	Σ_{SFR} ($\log M_\odot$ yr^{-1} kpc^{-2})	τ_{gas} (Gyr)	Morphology
214184	HATLASJ083601.5+002617	08:36:01.6	+00:26:18.1	0.0332	10.31 ± 0.02	2.06 ± 0.1	10.59 ± 0.1	0.05 ± 0.01	111.545	54 ± 11	306 ± 27	[b]20.6 ± 0.85	0.104 ± 0.004	9.68 ± 0.018	10.1 ± 0.8	0.43 ± 0.03	1.3 ± 0.3	−2.1 ± 0.3	2.318 ± 0.15	DB
3895257	HATLASJ083745.1−005141	08:37:45.2	−00:51:40.9	0.0306	10.13 ± 0.03	1.35 ± 0.09	10.35 ± 0.12	0.06 ± 0.02	111.843	18 ± 14	202 ± 33	[b]8.1 ± 0.62	0.034 ± 0.003	9.2 ± 0.034	6.4 ± 0.9	0.85 ± 0.09	1.3 ± 0.1	−2.0 ± 0.1	1.17 ± 0.119	D
208589	HATLASJ083831.9+000045	08:38:31.9	+00:00:45.0	0.0781	11.15 ± 0.01	14.17 ± 0.4	10.27 ± 0.11	0.77 ± 0.2	106.911	38 ± 3	172 ± 8	8.8 ± 0.68	0.25 ± 0.019	10.06 ± 0.034	6.6 ± 0.6	1.23 ± 0.1	1.2 ± 0.3	−2.1 ± 0.3	0.81 ± 0.067	DBC
345647	HATLASJ084139.5+015346	08:41:39.5	+01:53:46.7	0.0736	10.98 ± 0.01	9.48 ± 0.25	10.29 ± 0.11	0.49 ± 0.13	107.561			<1.3	<0.032							
417395	HATLASJ084217.7+021222	08:42:17.9	+02:12:23.4	0.096	10.93 ± 0.04	8.51 ± 0.79	10.53 ± 0.11	0.25 ± 0.07	105.185	−35 ± 5	186 ± 12	[b]5.7 ± 0.45	0.249 ± 0.02	10.059 ± 0.034	17.3 ± 1.4	0.74 ± 0.09	1.1 ± 0.2	−2.3 ± 0.2	1.346 ± 0.163	DBC
300757	HATLASJ084305.0+010858	08:43:05.1	+01:08:56.0	0.0777	11.05 ± 0.03	11.31 ± 0.78	10.41 ± 0.17	0.44 ± 0.17	106.975	−40 ± 4	187 ± 11	5.9 ± 0.6	0.166 ± 0.017	9.883 ± 0.044		1.48 ± 0.18			0.676 ± 0.083	DBC
371334	HATLASJ084350.7+005535	08:43:50.8	+00:55:34.8	0.0729	11.03 ± 0.01	10.61 ± 0.27	10.64 ± 0.12	0.24 ± 0.07	107.478	30 ± 17	283 ± 47	7.7 ± 0.64	0.191 ± 0.016	9.943 ± 0.036		1.21 ± 0.11			0.826 ± 0.072	DBC
345754	HATLASJ084428.3+020349	08:44:28.4	+02:03:49.8	0.0254	10.25 ± 0.01	1.8 ± 0.04	10.29 ± 0.12	0.09 ± 0.03	112.401	46 ± 4	203 ± 20	14.0 ± 1.18	0.041 ± 0.003	9.276 ± 0.037		0.95 ± 0.08			1.049 ± 0.091	DBC
386263	HATLASJ084428.3+020657	08:44:28.4	+02:06:57.4	0.0786	11.01 ± 0.03	10.33 ± 0.64	10.78 ± 0.11	0.17 ± 0.05	106.865	5 ± 10	349 ± 25	13.6 ± 1.78	0.392 ± 0.051	10.255 ± 0.057		0.57 ± 0.08			1.744 ± 0.253	DC
278475	HATLASJ084630.7+005055	08:46:30.9	+00:50:53.3	0.1323	11.51 ± 0.02	32.13 ± 1.69	10.36 ± 0.12	1.42 ± 0.39	101.802	−4 ± 9	324 ± 23	5.5 ± 0.5	0.463 ± 0.042	9.569 ± 0.039		8.67 ± 0.91			0.115 ± 0.012	M
3624571	HATLASJ084907.0−005139	08:49:07.1	−00:51:37.7	0.0698	11.18 ± 0.01	15.1 ± 0.33	10.48 ± 0.11	0.5 ± 0.13	107.752	−3 ± 4	244 ± 9	12.3 ± 0.98	0.279 ± 0.022	10.108 ± 0.035		1.18 ± 0.1			0.85 ± 0.07	BC
376293	HATLASJ085111.5+013006	08:51:11.4	+01:30:06.9	0.0594	10.72 ± 0.02	5.29 ± 0.26	10.56 ± 0.1	0.15 ± 0.04	108.805	16 ± 15	372 ± 35	[b]12.2 ± 0.46	0.198 ± 0.007	9.96 ± 0.016	13.9 ± 0.7	0.58 ± 0.04	1.0 ± 0.3	−2.1 ± 0.3	1.724 ± 0.107	DB
371789	HATLASJ085112.9+010342	08:51:12.8	+01:03:43.7	0.0267	10.2 ± 0.01	1.58 ± 0.04	10.14 ± 0.12	0.11 ± 0.03	112.28	−13 ± 4	143 ± 11	6.3 ± 0.87	0.02 ± 0.003	8.972 ± 0.06		1.68 ± 0.24			0.595 ± 0.083	DB
323772	HATLASJ085234.4+013419	08:52:33.9	+01:34:22.7	0.195	11.92 ± 0.01	83.43 ± 2.18	10.57 ± 0.12	2.25 ± 0.62	96.417	134 ± 16	340 ± 38	10.7 ± 0.07	1.999 ± 0.012	10.963 ± 0.003		0.91 ± 0.02			1.102 ± 0.03	BC
323855	HATLASJ085340.7+013348	08:53:40.7	+01:33:47.9	0.041	10.28 ± 0.03	1.92 ± 0.14	10.36 ± 0.12	0.08 ± 0.02	110.722	26 ± 14	140 ± 32	[b]8.0 ± 0.37	0.061 ± 0.003	9.451 ± 0.02	11.2 ± 2.3	0.68 ± 0.06	1.9 ± 0.3	−1.0 ± 0.3	1.471 ± 0.125	DC
600024	HATLASJ085346.4+001252	08:53:46.3	+00:12:52.4	0.0504	10.71 ± 0.01	5.11 ± 0.15	10.31 ± 0.12	0.25 ± 0.07	109.73	8 ± 12	259 ± 29	6.5 ± 0.13	0.076 ± 0.002	9.543 ± 0.009	5.5 ± 0.7	1.46 ± 0.05	2.0 ± 0.3	−1.2 ± 0.3	0.684 ± 0.025	D
600026	HATLASJ085356.5+001256	08:53:56.3	+00:12:56.3	0.0508	10.33 ± 0.03	2.14 ± 0.16	10.01 ± 0.12	0.21 ± 0.06	109.683	31 ± 5	138 ± 13	[b]5.7 ± 0.14	0.068 ± 0.002	9.493 ± 0.011	9.5 ± 2.5	0.69 ± 0.06	1.1 ± 0.2	−2.1 ± 0.2	1.45 ± 0.116	DB
301346	HATLASJ085406.0+011129	08:54:05.9	+01:11:30.4	0.0441	10.54 ± 0.02	3.5 ± 0.14	9.79 ± 0.13	0.57 ± 0.17	110.405	−5 ± 17	255 ± 41	4.8 ± 1.25	0.043 ± 0.011	9.295 ± 0.113	4.5 ± 1.2	1.77 ± 0.47	0.8 ± 0.2	−2.6 ± 0.2	0.564 ± 0.149	DBC
386720	HATLASJ085450.2+021207	08:54:50.2	+02:12:08.3	0.0583	10.7 ± 0.02	5.05 ± 0.27	10.66 ± 0.1	0.11 ± 0.03	108.909	29 ± 15	387 ± 36	12.9 ± 1.23	0.202 ± 0.019	9.969 ± 0.042	8.6 ± 0.8	0.54 ± 0.06	1.0 ± 0.1	−2.1 ± 0.1	1.842 ± 0.201	DB
278874	HATLASJ085615.9+005237	08:56:16.0	+00:52:36.2	0.1692	10.94 ± 0.01	8.62 ± 0.22	10.96 ± 0.1	0.09 ± 0.02	98.588	15 ± 13	252 ± 32	3.2 ± 0.55	0.443 ± 0.076	10.31 ± 0.075	17.1 ± 2.9	0.42 ± 0.07	1.1 ± 0.2	−2.5 ± 0.2	2.365 ± 0.411	B
600164	HATLASJ085623.6+001352	08:56:23.7	+00:13:51.7	0.1774	11.14 ± 0.01	13.86 ± 0.36	10.7 ± 0.12	0.27 ± 0.07	97.305			<0.8	<0.119							
622662	HATLASJ085748.0+004641	08:57:48.0	+00:46:38.7	0.0718	11.27 ± 0.01	18.68 ± 0.33	10.37 ± 0.11	0.79 ± 0.2	107.552	0 ± 2	182 ± 6	11.5 ± 0.58	0.276 ± 0.014	9.344 ± 0.022		8.46 ± 0.45			0.118 ± 0.006	M
376631	HATLASJ085750.0+012808	08:57:50.0	+01:28:06.7	0.1993	10.92 ± 0.01	8.38 ± 0.21	10.49 ± 0.12	0.27 ± 0.08	96.117			[a]0.3 ± 0.17	0.056	9.409		3.26			0.306	DB
301648	HATLASJ085828.4+012211	08:58:28.5	+01:22:11.5	0.1992	11.46 ± 0.01	29.15 ± 0.77	10.7 ± 0.12	0.58 ± 0.16	96.14			[a]0.4 ± 0.18	0.079	9.563		7.98			0.125	BD
622694	HATLASJ085828.5+003815	08:58:28.6	+00:38:14.8	0.0524	10.44 ± 0.02	2.72 ± 0.14	10.43 ± 0.11	0.1 ± 0.03	109.538	−6 ± 8	223 ± 19	3.4 ± 0.42	0.043 ± 0.005	9.301 ± 0.053	8.2 ± 0.8	1.36 ± 0.18	1.5 ± 0.3	−1.4 ± 0.3	0.734 ± 0.097	DBC
376679	HATLASJ085836.0+013149	08:58:36.0	+01:31:49.0	0.1068	11.22 ± 0.01	16.51 ± 0.43	10.9 ± 0.1	0.21 ± 0.05	104.131	57 ± 6	217 ± 15	[b]10.3 ± 0.2	0.554 ± 0.011	10.406 ± 0.008	24.9 ± 1.2	0.65 ± 0.02	1.4 ± 0.2	−1.6 ± 0.2	1.544 ± 0.051	DBC
382034	HATLASJ085957.9+015632	08:59:57.9	+01:56:34.2	0.1943	11.34 ± 0.01	21.69 ± 0.57	10.81 ± 0.2	0.33 ± 0.15	96.531			[a]0.5 ± 0.18	0.087	8.843		31.15			0.032	M
209807	HATLASJ090004.9+000447	09:00:05.0	+00:04:46.8	0.0539	10.57 ± 0.02	3.68 ± 0.15	10.7 ± 0.1	0.07 ± 0.02	109.375	14 ± 10	308 ± 24	11.4 ± 1.64	0.153 ± 0.022	9.848 ± 0.062		0.52 ± 0.08			1.916 ± 0.286	DBC
346900	HATLASJ090120.7+020224	09:01:20.7	+02:02:24.9	0.2009	11.28 ± 0.01	18.95 ± 0.49	11.06 ± 0.15	0.16 ± 0.06	95.954	95 ± 26	393 ± 62	4.0 ± 0.51	0.789 ± 0.101	10.56 ± 0.056	21.2 ± 5.0	0.52 ± 0.07	1.9 ± 0.2	−1.6 ± 0.2	1.916 ± 0.25	DBC
203879	HATLASJ090223.8−001639	09:02:23.8	−00:16:39.6	0.1963	10.94 ± 0.01	8.72 ± 0.22	11.03 ± 0.1	0.08 ± 0.02	96.338			[a]0.2 ± 0.17	0.032	9.166		5.95			0.168	BD
382362	HATLASJ090532.6+020220	09:05:32.6	+02:02:21.9	0.0519	10.69 ± 0.02	4.89 ± 0.17	10.8 ± 0.1	0.08 ± 0.02	109.59	−13 ± 16	256 ± 37	19.2 ± 4.08	0.238 ± 0.051	10.039 ± 0.092	6.8 ± 1.4	0.45 ± 0.1	1.6 ± 0.2	−1.3 ± 0.2	2.24 ± 0.483	DB
600656	HATLASJ090633.6+001526	09:06:33.6	+00:15:27.9	0.165	10.88 ± 0.01	7.66 ± 0.19	10.98 ± 0.11	0.08 ± 0.02	98.913	95 ± 22	334 ± 53	2.3 ± 0.1	0.301 ± 0.013	10.141 ± 0.019		0.55 ± 0.03			1.807 ± 0.092	DBC
279387	HATLASJ090750.0+010141	09:07:50.1	+01:01:41.8	0.1281	11.7 ± 0.01	50.07 ± 1.05	10.14 ± 0.12	3.62 ± 0.97	102.191	−22 ± 3	150 ± 7	6.8 ± 0.58	0.535 ± 0.045	9.631 ± 0.037		11.71 ± 1.02			0.085 ± 0.007	M

Table 2 – *continued*

GAMA ID	Source	RA (J2000)	Dec. (J2000)	z_{spec}	$\log[L_{IR}/L_{\odot}]$	SFR	$\log[M_*/M_{\odot}]$	sSFR	ν_{obs}	v_{obs}	v_{FWHM}	$S_{CO}\,\Delta v$	$L'_{CO}/10^{10}$	$\log[M_{H2}/M_{\odot}]$	R_{FWHM}	SFE	Σ_{gas}	Σ_{SFR}	τ_{gas}	Morphology
						$[M_{\odot}\ yr^{-1}]$		(Gyr^{-1})	(GHz)	$(km\ s^{-1})$	$(km\ s^{-1})$	$(Jy\ km\ s^{-1})$	$(K\ km\ s^{-1}\ pc^2)$		(kpc)	(Gyr^{-1})	$(\log M_{\odot}\ pc^{-2})$	$(\log M_{\odot}\ yr^{-1}\ kpc^{-2})$	(Gyr)	
324842	HATLASJ090949.6+014847	09:09:49.6	+01:48:46.0	0.1819	11.84 ± 0.02	68.47 ± 2.7	10.89 ± 0.12	0.88 ± 0.24	97.531	6 ± 1	73 ± 3	8.5 ± 0.58	1.364 ± 0.093	10.798 ± 0.03		1.09 ± 0.09			0.917 ± 0.072	BC
324931	HATLASJ091157.2+014454	09:11:57.2	+01:44:53.9	0.1694	11.39 ± 0.01	24.49 ± 0.64	10.9 ± 0.16	0.31 ± 0.11	98.569	-3 ± 5	168 ± 13	5.3 ± 0.52	0.737 ± 0.072	10.53 ± 0.043		0.72 ± 0.07			1.384 ± 0.141	DBC
216401	HATLASJ091205.8+002655	09:12:05.8	+00:26:55.6	0.0545	11.09 ± 0.01	12.32 ± 0.2	10.33 ± 0.11	0.58 ± 0.14	109.314	10 ± 2	171 ± 6	13.6 ± 0.84	0.187 ± 0.011	9.934 ± 0.027		1.44 ± 0.09			0.697 ± 0.044	BC
210543	HATLASJ091420.1+000509	09:14:20.0	+00:05:10.0	0.2022	11.55 ± 0.01	35.48 ± 0.94	10.62 ± 0.13	0.85 ± 0.25	95.874	37 ± 9	302 ± 22	3.3 ± 0.57	0.667 ± 0.114	10.487 ± 0.074		1.16 ± 0.2			0.864 ± 0.15	B
378002	HATLASJ091956.8+013851	09:19:57.0	+01:38:51.6	0.1764	11.13 ± 0.01	13.48 ± 0.35	10.45 ± 0.12	0.48 ± 0.13	97.994	-10 ± 7	151 ± 16	2.4 ± 0.32	0.365 ± 0.048	10.225 ± 0.057		0.8 ± 0.11			1.246 ± 0.168	BD
216973	HATLASJ092232.2+002707	09:22:32.3	+00:27:08.4	0.173	11.19 ± 0.01	15.6 ± 0.4	10.36 ± 0.12	0.68 ± 0.18	98.305	-96 ± 24	518 ± 57	3.5 ± 0.64	0.504 ± 0.093	10.366 ± 0.08		0.67 ± 0.12			1.487 ± 0.276	DC
30313	HATLASJ113740.6−010454	11:37:40.7	−01:04:54.1	0.1517	10.93 ± 0.01	8.49 ± 0.21	10.71 ± 0.12	0.17 ± 0.05	100.123			[a]0.9 ± 0.11	0.096	9.646		1.92			0.521	DB
53724	HATLASJ113858.4−001629	11:38:58.5	−00:16:30.2	0.1637	11.21 ± 0.01	16.12 ± 0.42	10.84 ± 0.12	0.23 ± 0.06	99.075	-58 ± 19	261 ± 45	4.2 ± 1.0	0.546 ± 0.129	10.4 ± 0.103	18.8 ± 4.2	0.64 ± 0.15	1.4 ± 0.1	-2.1 ± 0.1	1.559 ± 0.372	DBC
69661	HATLASJ114343.9+000203	11:43:44.1	+00:02:02.5	0.1872	11.05 ± 0.01	11.18 ± 0.28	10.1 ± 0.12	0.89 ± 0.25	97.106	-24 ± 4	67 ± 10	2.8 ± 0.52	0.485 ± 0.089	10.348 ± 0.08	18.0 ± 4.1	0.5 ± 0.09	1.5 ± 0.1	-1.8 ± 0.1	1.994 ± 0.369	BC
84183	HATLASJ114540.7+002554	11:45:41.0	+00:25:55.3	0.3429	11.56 ± 0.01	36.44 ± 0.97	11.04 ± 0.11	0.33 ± 0.09	85.827			[a]0.2 ± 0.18	0.147	9.831		5.38			0.186	DB
136959	HATLASJ114625.1−014511	11:46:25.0	−01:45:13.0	0.1645	11.72 ± 0.01	52.8 ± 1.42	10.71 ± 0.1	1.03 ± 0.24	98.956	95 ± 11	381 ± 28	6.6 ± 0.64	0.861 ± 0.084	10.598 ± 0.043		1.33 ± 0.14			0.75 ± 0.076	D
758786	HATLASJ114702.7+001207	11:47:02.8	+00:12:07.0	0.328	11.67 ± 0.01	46.3 ± 1.24	10.81 ± 0.11	0.71 ± 0.19	86.779	61 ± 32	335 ± 76	2.3 ± 0.72	1.279 ± 0.393	10.769 ± 0.134	35.0 ± 9.5	0.79 ± 0.24	2.5 ± 0.4	-0.5 ± 0.4	1.27 ± 0.392	D
30979	HATLASJ115039.6−010639	11:50:39.7	−01:06:40.7	0.343	11.93 ± 0.01	84.51 ± 2.32	11.3 ± 0.14	0.42 ± 0.14	85.84			[a]0.5 ± 0.18	0.284	10.117		6.46			0.155	B
39703	HATLASJ115141.3−004239	11:51:41.5	−00:42:39.5	0.321	11.77 ± 0.01	58.93 ± 1.6	10.94 ± 0.11	0.68 ± 0.17	87.265			[a]1.1 ± 0.16	0.548	10.402		2.34			0.428	B
535507	HATLASJ115317.4−010123	11:53:17.4	−01:01:21.3	0.1804	11.18 ± 0.01	15.13 ± 0.39	10.73 ± 0.19	0.28 ± 0.12	97.661	-21 ± 45	506 ± 107	3.3 ± 0.76	0.526 ± 0.12	10.384 ± 0.099		0.62 ± 0.14			1.6 ± 0.368	BD
179053	HATLASJ121141.8−015731	12:11:41.8	−01:57:29.7	0.317	11.8 ± 0.01	63.65 ± 1.73	11.18 ± 0.1	0.42 ± 0.09	87.599			[a]0.4 ± 0.17	0.21	9.984		6.6			0.152	B
186110	HATLASJ121206.2−013425	12:12:06.2	−01:34:24.3	0.1588	10.77 ± 0.01	5.84 ± 0.14	10.86 ± 0.11	0.08 ± 0.02	99.604			<0.9	<0.108							
55717	HATLASJ121253.5−002203	12:12:53.5	−00:22:04.4	0.1855	11.11 ± 0.01	13.01 ± 0.33	10.79 ± 0.11	0.21 ± 0.05	97.238	-8 ± 12	202 ± 28	2.7 ± 0.39	0.447 ± 0.065	10.313 ± 0.063		0.63 ± 0.09			1.581 ± 0.234	DB
99611	HATLASJ121427.4+005818	12:14:27.4	+00:58:18.3	0.184	11.27 ± 0.01	18.44 ± 0.48	10.93 ± 0.13	0.22 ± 0.06	97.34	41 ± 9	215 ± 22	2.8 ± 0.42	0.46 ± 0.069	9.566 ± 0.065		5.01 ± 0.77			0.2 ± 0.03	MBC
32169	HATLASJ121446.4−011155	12:14:46.5	−01:11:55.6	0.1797	11.55 ± 0.01	35.36 ± 0.94	10.82 ± 0.11	0.54 ± 0.14	97.707	13 ± 19	402 ± 47	4.6 ± 0.6	0.725 ± 0.094	10.523 ± 0.056		1.06 ± 0.14			0.944 ± 0.125	BC
537340	HATLASJ121908.8−010201	12:19:08.8	−01:02:00.5	0.1575	10.89 ± 0.01	7.76 ± 0.19	11.12 ± 0.11	0.06 ± 0.01	99.635			[a]0.5 ± 0.18	0.061	9.447		2.77			0.361	B
543473	HATLASJ140649.0−005647	14:06:49.0	−00:56:47.9	0.2715	11.66 ± 0.01	45.51 ± 1.22	11.25 ± 0.12	0.25 ± 0.07	90.656	12 ± 36	390 ± 86	2.3 ± 0.52	0.834 ± 0.192	10.584 ± 0.1		1.19 ± 0.28			0.843 ± 0.196	BD
491545	HATLASJ140912.3−013454	14:09:12.5	−01:34:54.9	0.2649	11.89 ± 0.01	78.16 ± 2.14	10.97 ± 0.13	0.84 ± 0.26	91.098	100 ± 11	271 ± 27	4.3 ± 0.66	1.494 ± 0.231	10.837 ± 0.067		1.14 ± 0.18			0.879 ± 0.138	BC
105572	HATLASJ141008.0+005106	14:10:08.0	+00:51:06.9	0.2564	11.83 ± 0.01	67.9 ± 1.85	11.1 ± 0.12	0.54 ± 0.15	91.702	144 ± 29	411 ± 70	4.0 ± 0.9	1.311 ± 0.295	10.78 ± 0.098	13.7 ± 3.6	1.13 ± 0.26	1.8 ± 0.2	-1.5 ± 0.2	0.888 ± 0.201	BD
15049	HATLASJ141522.0+004413	14:15:22.1	+00:44:14.9	0.2682	11.37 ± 0.01	23.69 ± 0.62	10.84 ± 0.14	0.34 ± 0.11	90.928	-48 ± 90	805 ± 213	1.7 ± 0.45	0.614 ± 0.162	10.451 ± 0.114	22.7 ± 3.3	0.84 ± 0.22	1.4 ± 0.1	-1.9 ± 0.1	1.193 ± 0.315	BDC
227768	HATLASJ141908.4+011313	14:19:08.6	+01:13:10.7	0.2801	11.52 ± 0.01	33.23 ± 0.88	11.0 ± 0.11	0.33 ± 0.09	90.11			<0.8	<0.321							
511560	HATLASJ141925.3−011130	14:19:25.4	−01:11:30.5	0.2533	11.75 ± 0.01	56.6 ± 1.53	10.15 ± 0.12	4.03 ± 1.16	91.991			[a]0.3 ± 0.16	0.091	9.62		13.58			0.074	BDC
319660	HATLASJ142057.9+015233	14:20:58.0	+01:52:32.1	0.2646	11.64 ± 0.01	43.85 ± 1.18	10.86 ± 0.12	0.6 ± 0.17	91.145	19 ± 15	244 ± 37	3.5 ± 0.66	1.238 ± 0.231	10.755 ± 0.081	15.4 ± 0.8	0.77 ± 0.15	2.0 ± 0.1	-1.5 ± 0.1	1.298 ± 0.245	BDC
106336	HATLASJ142208.8+005428	14:22:09.0	+00:54:27.4	0.2541	11.46 ± 0.01	28.77 ± 0.76	11.17 ± 0.13	0.19 ± 0.06	91.953	-117 ± 26	261 ± 63	2.6 ± 0.16	0.822 ± 0.051	9.818 ± 0.027		4.38 ± 0.3			0.229 ± 0.016	MC
228157	HATLASJ142517.1+010546	14:25:17.1	+01:05:46.6	0.2807	11.84 ± 0.01	68.52 ± 1.87	11.07 ± 0.12	0.58 ± 0.16	90.023	-52 ± 12	308 ± 29	4.3 ± 0.6	1.714 ± 0.237	10.897 ± 0.06		0.87 ± 0.12			1.151 ± 0.162	BD
771527	HATLASJ144116.3+002724	14:41:16.4	+00:27:26.0	0.2441	11.08 ± 0.01	12.16 ± 0.31	10.83 ± 0.11	0.18 ± 0.05	92.647			<0.9	<0.262							
594509	HATLASJ144129.5−000902	14:41:29.7	−00:09:01.2	0.2432	11.25 ± 0.01	17.84 ± 0.46	10.98 ± 0.13	0.19 ± 0.06	92.688			<0.9	<0.261							
93478	HATLASJ144218.7+003615	14:42:18.7	+00:36:15.5	0.2409	11.55 ± 0.01	35.27 ± 0.94	10.58 ± 0.12	0.92 ± 0.25	92.859	112 ± 18	363 ± 42	3.5 ± 0.96	1.014 ± 0.276	10.669 ± 0.118		0.76 ± 0.21			1.322 ± 0.362	B
16985	HATLASJ144515.0+003907	14:45:15.1	+00:39:06.4	0.2818	11.85 ± 0.01	70.93 ± 1.94	10.85 ± 0.15	1.01 ± 0.36	89.886			[a]0.6 ± 0.17	0.239	9.282		37.04			0.027	M

Notes. [a]These sources were spectroscopically undetected, and their fluxes were computed from collapsed cubes (between $\nu_{obs} \pm \langle \upsilon_{FWHM} \rangle$) using a 2D Gaussian fit with task GAUSSFIT.
[b]These are extended sources. Velocity-integrated flux densities have been calculated over an irregular region covering the whole extension of the emission.

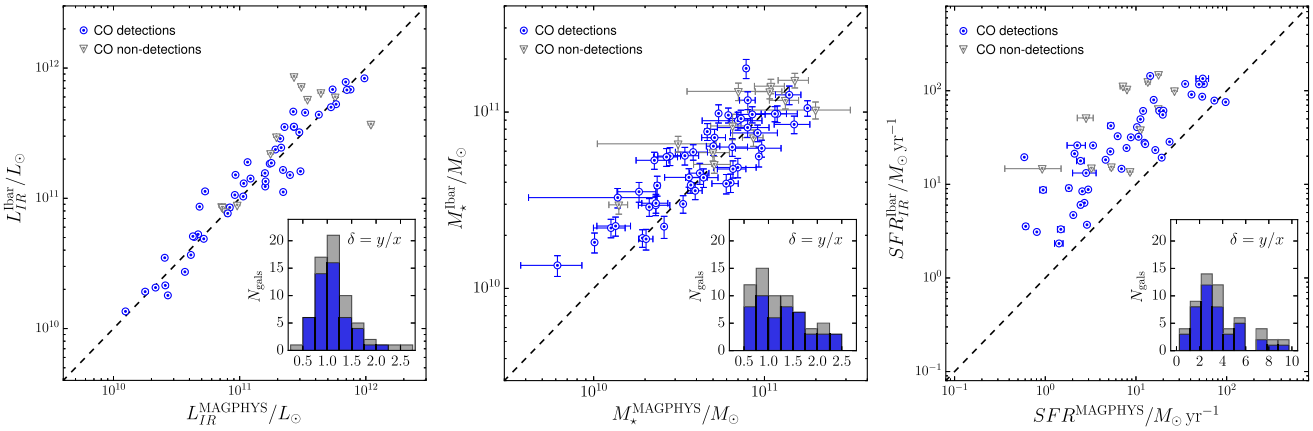

Figure 3. Comparing the infrared luminosity (*left*), stellar mass (*middle*) and SFR (*right*) derived from empirical methods (see Ibar et al. 2015) with those obtained from the MAGPHYS UV–submm SED fitting (see Driver et al. 2016).

2.4.3 *SED fitting*

All of our galaxies are present in the GAMA Panchromatic Data Release[6] (Driver et al. 2016) that provides imaging for over 230 deg^2 with photometry in 21 bands extending from the far-ultraviolet to far-infrared from a range of facilities that currently includes the GALaxy Evolution eXplorer (*GALEX*), SDSS, Visible and Infrared Telescope for Astronomy (VISTA), WISE and *Herschel*, meaning that the SED between 0.1 and 500 μm is available for each galaxy. These observed rest-frame SEDs have all been modelled with the Bayesian SED fitting code, MAGPHYS (da Cunha, Charlot & Elbaz 2008), which fits the panchromatic SED from a library of optical and infrared SEDs derived from a generalized multicomponent model of a galaxy, whilst giving special consideration to the dust–energy balance. Although Driver et al. (in preparation) will present a complete catalogue and analysis of all the GAMA SEDs modelled with MAGPHYS and the corresponding best-fitting model parameters (see also Hughes et al. 2017a), in our present study we use the derived stellar masses and their uncertainties, which we calculate from the upper (16th percentile) and lower (84th percentile) limits of the probability distribution function associated with the stellar mass given by the best-fitting model, as presented in Table 2.

We briefly assess the quality of the fitting by comparing the stellar masses and IR luminosities derived from MAGPHYS to those estimates from our previous study presented in Ibar et al. (2015). Both of these parameters demonstrate satisfactory agreement with a mean scatter of between 0.15 and 0.2 dex (see Fig. 3). In contrast, our derived SFRs show a constant systematic offset across the parameter range (of a factor of 2, where MAGPHYS are lower than those estimates from Ibar et al. 2015 using $L_{\rm IR}$), which likely arises from differences in SFR definition/calibration (see e.g. Kennicutt & Evans 2012). However, removing this systematic offset yields a mean scatter of 0.2 dex.

2.4.4 *Morphological properties*

In order to explore the morphological properties of our galaxies, we use the GAMA Panchromatic Swarp Imager[7] to extract multi-wavelength imaging from *GALEX*, SDSS, VISTA and WISE. We classify each source (based on visual inspection agreed by four members of our team) into three different categories according to the prominence of key morphological features: a Bulge ('B'), Disc ('D') and Merger-Irregular ('M'). If the source presents more than one morphology, we mark the first letter as the dominant morphology. If the source has multiple neighbouring systems, then we add 'C' to denote these 'companions'. In the following, we refer to our galaxies as 'B', 'D' or 'M' dominated galaxies. We also note that this morphological classification is used to define the most suitable $\alpha_{\rm CO}$ to then compute $M_{\rm H_2}$ (this is discussed in Section 3.2).

3 RESULTS AND DISCUSSION

3.1 Morphological description

We have made a census for the different optical/near-IR morphologies present in our sample, according to the morphological classification scheme explained in Section 2.4.4. From a total of 49 spectrally detected sources, we have identified 18 as B-dominated, 26 as D-dominated and 5 as M-dominated galaxies (see the morphology column in Table 2). By definition, the five M-dominated galaxies present signs of possible morphological disruption: three galaxies are clear interacting system (with two or more companions) and two show traces of the late stages of merger events. In the case of the spectrally undetected galaxies, we have identified 11 as B-dominated, 4 as D-dominated and 3 as M-dominated galaxies. We do not identify any clear morphological difference between CO-detected and CO-undetected galaxies.

ALMA observations spatially resolve the CO emission in 21 galaxies (see Section 2.4.1). We calculate the deconvolved FWHM of the semimajor axis ($R_{\rm FWHM}$) using the task GAUSSFIT (within CASA), finding CO sizes in the range of 3.4–15.2 arcsec (3.7–35.0 kpc in physical units), usually resolved at a significance of $\sim 7\sigma$ (median value). We compare the optical and CO sizes by using the Petrosian radius in r band ($R_{\rm P,Opt}$) and the Petrosian radius in CO ($R_{\rm P,CO}$), using equation (1) from Shimasaku et al. (2001). We find values for $R_{\rm P,CO}$ in the range of 1.9–5.3 arcsec (2.8–14.0 kpc), with an average of 3.6 arcsec (6.7 kpc). For our sample, we find that the mean and scatter of the $R_{\rm P,Opt}/R_{\rm P,CO}$ distribution are 1.6 ± 0.5 (i.e. the CO emission is typically smaller than the stellar; see Fig. 4). Previous studies have shown a CO-to-optical ratio of unity for 'main-sequence' galaxies, locally (e.g. Young et al. 1995; Regan et al. 2001; Leroy et al. 2008)

[6] http://gama-psi.icrar.org
[7] http://gama-psi.icrar.org/psi.php

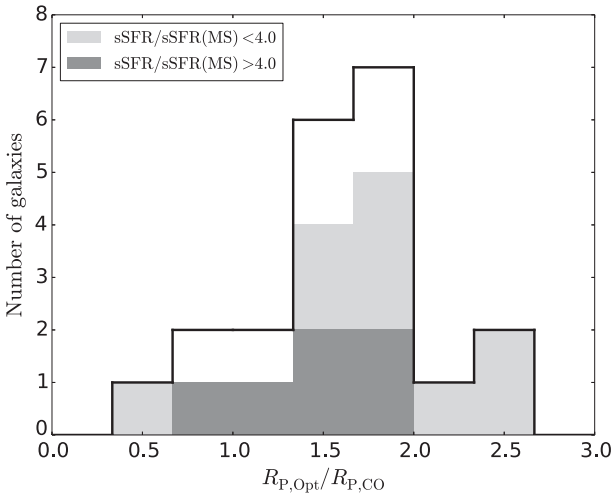

Figure 4. The ratio between the Petrosian radius in r band ($R_{\rm P,Opt}$) and CO ($R_{\rm P,CO}$) for the 21 ALMA-resolved sources. We separate our sample into two populations based on the relative levels of starburst activity (see Fig. 1). We find that most of our galaxies are distributed around a size ratio ∼1.3–2.0.

and at high-z (e.g. Tacconi et al. 2013; Bolatto et al. 2015). In a different luminosity range, Simpson et al. (2015) found that the sizes of SMGs at $z = 2.6$–4 in optical *HST* imaging are around four times larger than in CO. Taking into account the typical values of sSFR/sSFR(MS) for our 21 resolved galaxies, we explore if the optical-to-CO ratio changes as a function of sSFR. We perform a Kolmogorov–Smirnov for both 'main sequence' and 'starburst' $R_{\rm P,Opt}/R_{\rm P,CO}$ populations (using sSFR/sSFR$_{\rm MS} = 4.0$ as a threshold; see the definition of 'main-sequence' in Fig. 1), finding a 90 per cent probability that both populations come from the same parent distribution (see Fig. 4). This little difference might be a product of the small deviation seen from the main sequence ('starburstiness') or the six spatially resolved starburst galaxies presented here.

3.2 Correlations between $L_{\rm IR}$ and $L'_{\rm CO}$

We compute the CO luminosity following Solomon & Vanden Bout (2005),

$$L'_{\rm CO} = 3.25 \times 10^7 S_{\rm CO}\,\Delta v\,\nu_{\rm obs}^{-2}\,D_{\rm L}^2\,(1+z)^{-3}\ ({\rm K\,km\,s^{-1}\,pc^2}), \quad (2)$$

where $S_{\rm CO}\,\Delta v$ is the velocity-integrated flux density in units of Jy km s^{-1}, $\nu_{\rm obs}$ is the observed frequency of the emission line in GHz, $D_{\rm L}$ is the luminosity distance in Mpc and z is the redshift. We find that the values for $L'_{\rm CO}$ are in the range of (0.03–1.31) $\times\ 10^{10}$ K km s^{-1} pc^2, with a median of (0.3 $\pm$ 0.1) $\times\ 10^{10}$ K km s^{-1} pc^2 (see Fig. 5). We note that our survey expands the parameter space explored before by previous similar studies, such as: Combes et al. (2011) at (0.3–7) $\times\ 10^{10}$ K km s^{-1} pc^2; Braun et al. (2011) at (4–9) $\times\ 10^{10}$ K km s^{-1} pc^2; Magdis et al. (2014) at (0.5–2) $\times\ 10^{10}$ K km s^{-1} pc^2. Based on the IR luminosities derived from the *H*-ATLAS photometry (Section 2.4.2), we find that the ratios between $L_{\rm IR}$ and $L'_{\rm CO}$ are similar to those found in normal local SFGs (e.g. COLDGASS; Saintonge et al. 2011). However, our galaxies have smaller $L_{\rm IR}/L'_{\rm CO}$ ratio than typical (U)LIRGs in the same redshift range by a factor of ∼10 (see right-hand panel of Fig. 5). We compute a linear regression (in log scale) to the $L_{\rm IR}$ versus $L'_{\rm CO}$ relation for our spectrally detected B- and D-dominated galaxies, finding:

$$\log[L_{\rm IR}/{\rm L_\odot}] = (0.95 \pm 0.04) \times \log L'_{\rm CO}/({\rm K\,km\,s^{-1}\,pc^2}) + (2.0 \pm 0.4). \quad (3)$$

This parametrization is within 1σ of the value previously presented by Daddi et al. (2010b), and supports the clear linearity between these two quantities. However, this slope is steeper compared with

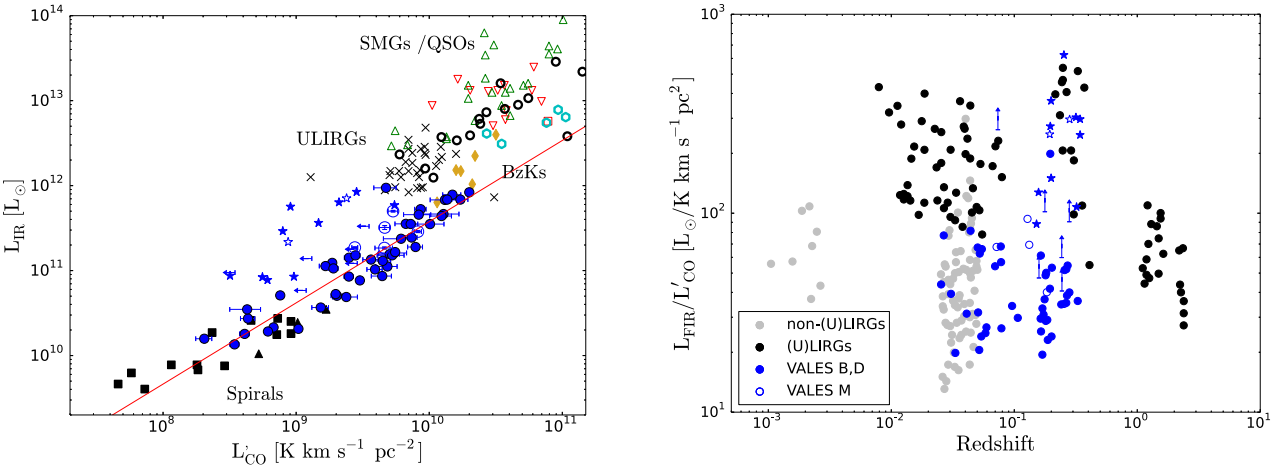

Figure 5. *Left:* Comparison of the CO and IR luminosities for our spectrally detected (blue circles), spectrally undetected but measured with low signal to noise in collapsed cubes (stars) and undetected (blue arrows) CO galaxies. Blue filled symbols are B- and D-dominated, while blue unfilled symbols are M-dominated galaxies. Our sample is compared to other studies taken from the literature, including: colour-selected galaxies (BzK; Daddi et al. 2010a; gold diamonds), submillimetre galaxies (SMGs; Greve et al. 2005, Daddi et al. 2009a,b; red down triangles, Frayer et al. 2008; blue empty square, Ivison et al. 2011; unfilled cyan hexagons), quasi-stellar objects (QSOs; Solomon & Vanden Bout 2005; Riechers et al. 2006; green empty triangles), local ULIRGs (Solomon et al. 1997; black crosses), local spirals (Leroy et al. 2008, 2009; black filled squares, Wilson et al. 2009; black filled triangles) and strongly lensed high-redshift dusty galaxies (Aravena et al. 2016; black unfilled circles). The solid line shows the best-fitting $L'_{\rm CO}$ versus $L_{\rm IR}$ relation for the detected B- and D-dominated galaxies presented in this work (see equation 3). *Right:* $L_{\rm IR}/L'_{\rm CO}$ as function of redshift. Our galaxies (blue symbols) and other relevant populations classified as (U)LIRGs (black circles) and non-(U)LIRGs (grey circles) taken from Magdis et al. (2012), including; local spirals (COLDGASS Saintonge et al. 2011); local ULIRGs (Solomon et al. 1997); $z \sim 0.3$ discs (Geach et al. 2011), *IRAS*-selected $z \sim 0.3$ ULIRGs (Combes et al. 2011) and high-z SFGs (Daddi et al. 2010a; Genzel et al. 2010).

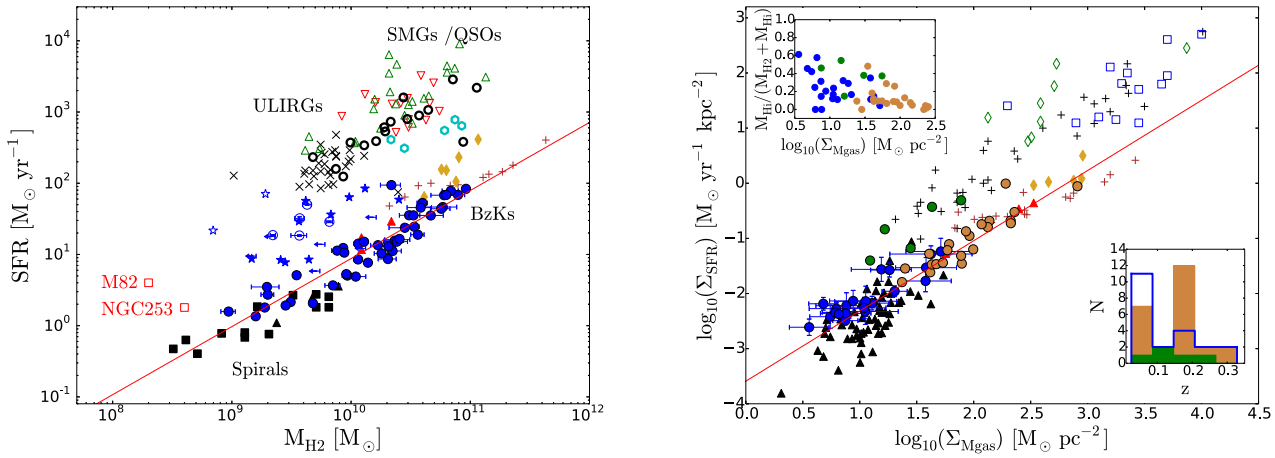

Figure 6. *Left*: The SFR versus $M_{\rm H_2}$ for our galaxies compared to previous works taken from the literature (assuming a Chabrier's IMF but considering the same $\alpha_{\rm CO}$ used in the original works). We show our spectrally detected (blue circles), spectrally undetected but measured with low signal to noise in collapsed cubes (stars) and undetected (blue arrows) CO galaxies (see Section 2.4 for details). Blue filled symbols are B- and D-dominated galaxies, while blue unfilled symbols are M-dominated galaxies. Figure contains BzK galaxies (Daddi et al. 2010a; gold diamonds), $z\sim0.5$ disc galaxies (Salmi et al. 2012; red filled triangles), $z=1$–2.3 normal galaxies (Tacconi et al. 2010; brown crosses), SMGs (Greve et al. 2005; Frayer et al. 2008; Daddi et al. 2009a,b; red down triangles, Ivison et al. 2011; unfilled cyan hexagons), QSOs (Riechers et al. 2006; green triangles), local ULIRGs (Solomon et al. 1997; black crosses), strongly lensed high-redshift dusty SFGs (Aravena et al. 2016; black unfilled circles) and local spirals (Leroy et al. 2009; black filled squares, Wilson et al. 2009; black filled triangles). M82 and NGC 253 are also shown (Houghton et al. 1997; Weiß et al. 2001; Kaneda et al. 2009). The solid red line is the best fit for the B- and D-dominated galaxies presented in this work (see equation 4). *Right*: The SFR surface density as a function of the gas mass (atomic and molecular) surface density for the 21 detected sources that can be spatially resolved in CO (blue circles; see Section 3.3), 23 detected B- and D-dominated that are unresolved in CO but resolved in *R* band (brown circles), and M-dominated unresolved in CO galaxies (green circles). Filled triangles are (U)LIRGS and spiral galaxies from the sample of Kennicutt (1998), brown crosses are $z=1$–2.3 normal galaxies (Tacconi et al. 2010). The empty blue squares and light green diamonds are SMGs from Bouché et al. (2007) and Bothwell, Kennicutt & Lee (2009), respectively. The red line is the best linear fit to all of our B- and D-dominated galaxies (see equation 6). The inset figures at the upper left and bottom right corners are as follows: (1) the relative contribution estimated by $M_{\rm H\,I}$ (following equation 5) to the total gas mass ($M_{\rm H_2}+M_{\rm H\,I}$) versus $\Sigma_{M_{\rm gas}}$. This figure demonstrates the decreasing effect that $M_{\rm H\,I}$ has at $\Sigma_{M_{\rm gas}}>10\,{\rm M_\odot\ pc^{-2}}$; (2) the redshift distribution of our VALES galaxies (blue, yellow and green circles), clearly showing that most of the spatially unresolved galaxies are the ones that are more distant.

that found by Ivison et al. (2011) in high-z SMG, local ULIRGs and LIRGs (∼0.5–0.7). We confirm that most of our detected galaxies (blue circles in left-hand panel of Fig. 5) follow the so-called 'sequence of discs', associated to a long-standing mode of star formation. We remark, however, that if we include in the statistics those galaxies that are not spectrally detected in CO (blue stars in left-hand panel of Fig. 5), although have low signal-to-noise emission in collapsed (moment 0 maps), the scatter in the correlation significantly increases. This indicates that deeper observations are required to provide details for the co-existence of different modes of star formation. We suggest that within the $L_{\rm IR}=10^{11-12}\,{\rm L_\odot}$ range, there might be a break (or a significant increment of the scatter) of the linear relation between the CO and far-IR luminosities (Sargent et al. 2014).

If we add into the statistics all samples presented in Fig. 5, in addition to our B- and D-dominated galaxies, we find in equation (3) a slope and normalization of 0.99 ± 0.02 and 1.7 ± 0.2, respectively. Although these parameters are in agreement with previous studies (slope ∼1.0–1.3; e.g. Daddi et al. 2010b; Genzel et al. 2010), we should highlight the growing evidence that the star formation efficiencies increase with redshift (e.g. Rowlands et al. 2014; Santini et al. 2014; Genzel et al. 2015; Scoville et al. 2016), therefore combining galaxy samples at different epochs might be an oversimplification of the analysis (see Fig. 5).

For those spectrally identified CO galaxies, we do not identify any clear variation of the $L_{\rm IR}/L'_{\rm CO}$ ratio as a function of redshift (up to $z=0.35$; see right-hand panel of Fig. 5). Our results are consistent with previous works that have shown a constant average $L_{\rm IR}/L'_{\rm CO}$ in 'main-sequence' galaxies up to $z\sim0.5$ (e.g. Santini et al. 2014). The scatter on the $L_{\rm IR}/L'_{\rm CO}$ ratio, however, increases if non-spectrally detected galaxies are included, an effect that is mainly dominated by the $0.15<z<0.35$ galaxy population.

Using $L'_{\rm CO}$, we compute the molecular gas mass ($M_{\rm H_2}$) assuming an $\alpha_{\rm CO}$ conversion factor dependent on the morphological classification (see Section 2.4.4). We adopt $\alpha_{\rm CO}=4.6$ (K km s^{-1} pc^2)$^{-1}$ for the B- and D-dominated galaxies (which includes contribution of He; Solomon & Vanden Bout 2005), while $\alpha_{\rm CO}=0.8$ (K km s^{-1} pc^2)$^{-1}$ for mergers/interacting galaxies. For B- and D-dominated galaxies, we find $M_{\rm H_2}$ values in the range of $\log(M_{\rm H_2}/{\rm M_\odot})=8.9$–$10.9$ with a median of $\log(M_{\rm H_2}/{\rm M_\odot})=10.31\pm0.1$, while for M-dominated galaxies values are in the range of $\log(M_{\rm H_2}/{\rm M_\odot})=9.3$–$9.8$ with a median of $\log(M_{\rm H_2}/{\rm M_\odot})=9.6\pm0.2$.

Performing a linear regression to the SFR versus $M_{\rm H_2}$ using our B- and D-dominated galaxies, we obtain

$$\log[{\rm SFR}/{\rm M_\odot\,yr^{-1}}]=(0.95\pm0.04)\times\log(M_{\rm H_2}/[{\rm M_\odot}])-(8.6\pm0.5). \quad (4)$$

In this work, we significantly increase the number of previously detected galaxies at $\log[M_{\rm H_2}/{\rm M_\odot}]\sim9$–$11$. Our sample complements the 'gap' between local spirals and 'normal' high-z colour-selected galaxies (Fig. 6). We note that our M-dominated galaxies are shifted towards higher SFRs, and closer to the local ULIRGs described by Solomon et al. (1997). At lower redshifts almost all galaxies follow a tight relationship between SFR and $\rm M_{H2}$, nevertheless we identify that galaxies at the upper side of the redshift distribution ($0.15<z<0.35$) tend to show a higher scatter

in this correlation. The scatter is larger when low signal-to-noise detections are included (see stars in left-hand panel of Fig. 6). If we combine our observations with all samples shown in the left-hand panel of Fig. 6), then in equation (4) we obtain a slope of 1.08 ± 0.02 with a normalization of -9.8 ± 0.2.

In both cases, one of the main factors controlling the scatter of the correlation is the different $\alpha_{\rm CO}$ conversion factor chosen for M-dominated galaxies. It is worth pointing out that deeper ALMA observations to spectrally detect the CO emission for all of our galaxies would probably confirm a population of optically unresolved ULIRGs-like galaxies with high star formation efficiencies (filling the 'gap' between spirals and ULIRGs local galaxies). As shown in left-hand panel of Fig. 5 (see blue stars), this population could significantly affect the slope and the scatter of the correlation.

The major uncertainty in our molecular gas mass estimates originates from the assumption of the $\alpha_{\rm CO}$ conversion factor. Indeed, assuming a different $\alpha_{\rm CO}$ can change $\rm M_{H2}$ by over a factor of six (around 500 times higher than observational errors). On the other hand, considering the metallicity range of our sample ($12 + \log_{10}(\rm O/H) = 8.7$–$9.2$; Ibar et al. 2015) and using the $\alpha_{\rm CO}$ parametrization for SFGs made by (Genzel et al. 2015, see their equation 8), we find that the $\alpha_{\rm CO}$ could vary by a factor of four with a tendency to lower values than 4.6 $(\rm K\ km\ s^{-1}\ pc^2)^{-1}$. In the left-hand panel of Fig. 6, galaxies can be shifted in position using a different $\alpha_{\rm CO}$, producing an artificial bimodal behaviour for the star formation activity in these galaxies. This can clearly affect the reliability for the existence of 'disc' and 'starburst' sequences. In Molina et al. (in prep.), we use kinematic arguments to confront the bimodality of the $\alpha_{\rm CO}$ conversion factor (e.g. Downes & Solomon 1998b; Sandstrom et al. 2013).

3.3 The Schmidt–Kennicutt relation

We introduce $M_{\rm gas} = M_{\rm H_2} + M_{\rm HI}$ as the total mass content in molecular and atomic gas. As we do not have direct $M_{\rm HI}$ observations, we estimate these using equation (4) from Zhang et al. (2009):

$$\log[M_{\rm HI}/M_\star] = -1.732\,38\,(g-r) + 0.215\,182\,\mu_i - 4.084\,51, \quad (5)$$

where g and r are the photometric magnitudes in those filters, and μ_i is the i-band surface brightness (SDSS filters). This approximation provides a 0.31 dex scatter for the estimate. For our sample, using equation (5) we find that the contribution is in general small (although non-negligible) with a mean ratio of $M_{\rm HI}/M_{\rm H_2} \sim 0.2$ (see Fig. 6).

Our 49 spectrally detected CO sources have SFRs in the range of 1–94 $\rm M_\odot\ yr^{-1}$, with a median value of $15 \pm 1\ \rm M_\odot\ yr^{-1}$. For those that are spatially resolved in CO (21 in total), we estimate the SFR and $M_{\rm gas}$ surface densities by dividing the measured values by the area of a two-sided disc ($2\pi R^2_{\rm FWHM}$), where $R_{\rm FWHM}$ is the deconvolved FWHM of the semimajor axis measured in ALMA CO images (see Table 2). In Fig. 6 (right), we show the Schmidt–Kennicutt relation (Schmidt 1959; Kennicutt 1998) comparing our samples with previous ones taken from the literature.

For those spectrally detected and spatially resolved CO galaxies, we obtain values for $\log[\Sigma_{\rm SFR}/(\rm M_\odot\ yr^{-1}\ kpc^{-2})]$ in the range of -2.61 and -1.23 , with a median of -2.18 ± 0.1 . Most of the spatially resolved ones (16) are D dominated while the rest (5) are B-dominated galaxies. The B- and D-dominated galaxies have on average three times higher $\Sigma_{\rm SFR}$ than local spiral galaxies, but around 30–70 times lower values than normal BzK galaxies at high-z. On the other hand, for the same spectrally detected CO galaxies, $\log[\Sigma_{M_{\rm gas}}/(\rm M_\odot\ pc^{-2})]$ values range between 0.55 and 1.71 , with a median value of 1.04 ± 0.29 . In terms of CO emission, we do not find any remarkable difference between our B- and D-dominated galaxies (although they do have different morphological optical features); the sample has on average two times greater $\Sigma_{M_{\rm gas}}$ than local spiral galaxies.

According to estimations of the molecular and atomic gas content in nearby galaxies (Bigiel & Blitz 2012), there is a strong evidence that the atomic gas saturates in column gas densities higher than $\sim 10\ \rm M_\odot\ pc^{-2}$. This is attributed to a natural threshold for the atomic to molecular gas transitions (Krumholz, McKee & Tumlinson 2009; Sternberg et al. 2014). As shown in Fig. 6, our atomic gas estimates decrease as a function of $\Sigma_{M_{\rm gas}}$ (as expected by the $M_{\rm HI}$ saturation), although the large scatter dominating equation (5) still predicts a non-negligible fraction of atomic gas above $\Sigma_{M_{\rm gas}} > 10^{10}\ \rm M_\odot\ pc^{-2}$.

Something to highlight is that left-hand and right-hand panels of Fig. 6 should behave similarly, nevertheless we find that most of our galaxies (blue circles) that are lying near the BzK population disappear after considering our spatially resolved CO selection criterion. To explore this further, we compare the median values of $M_{\rm H_2}$ and $R_{\rm CO}$ using resolved galaxies (in CO) at different redshift bins (centred at 0.07 and 0.2) in order to identify a possible evolution in physical size and mass of gas content. Previous studies have shown that at fixed $M_\star$ the averaged effective radius vary as $R_{\rm eff} \propto (1+z)^{-0.8}$ (Magdis et al. 2012). If we assume that the stars and the molecular gas follow the same spatial distribution (which is actually not the case; see Fig. 4), the measured CO sizes are expected to decrease by a factor of 1.1 between $z = 0.07$ and $z = 0.2$. This variation is not sufficient to explain what we observe in Fig. 6.

Considering the results coming from Section 3.1 to estimate $\Sigma_{\rm SFR}$ and $\Sigma_{M_{\rm gas}}$ for spatially unresolved CO galaxies, we used the Petrosian optical radius divided by the mean $R_{\rm P,\,Opt}/R_{\rm P,\,CO} = 1.6$ ratio found for our galaxies (note that $R_{\rm FWHM}$ and $R_{\rm P,\,CO}$ differ by only ~ 2 per cent). Brown and green circles in Fig. 6 correspond to CO-unresolved B-/D-dominated and M-dominated galaxies, respectively. The inset panel in Fig. 6 shows clearly that most of the spatially unresolved CO galaxies are those that are more distant (at $0.15 < z < 0.35$). This analysis demonstrates that our sample perfectly complements the parameter space in the Schmidt–Kennicutt relation that joins the local spiral galaxies with those 'normal' at high-z.

Using our data, we perform a linear regression in Fig. 6 using all B-/D-dominated galaxies that are spatially resolved in CO (21 sources) and unresolved in CO but resolved in the optical (23 sources). Being aware of the possible biases introduced by our H I estimates, we provide a parametrization for two cases; $M_{\rm H_2}$ and $M_{\rm gas}$,

$$\frac{\Sigma_{\rm SFR}}{\rm M_\odot\ yr^{-1}\ kpc^{-2}} = \begin{cases} (1.16 \pm 0.05) \times \log[\Sigma_{\rm M_{gas}}/\rm M_\odot\ pc^{-2}] \\ \quad -(3.3 \pm 0.1) \\ (1.27 \pm 0.05) \times \log[\Sigma_{\rm M_{H_2}}/\rm M_\odot\ pc^{-2}]. \\ \quad -(3.6 \pm 0.1) \end{cases} \quad (6)$$

These results are consistent with previously analyses using ensembles of clumps composing galaxies at $z = 1$–2 (e.g. Freundlich et al. 2013; Genzel et al. 2013) and star-forming discs with near-solar metallicities (slope $\sim 1.0 - 1.3$; e.g. Bigiel et al. 2008; Kennicutt et al. 2008; Leroy et al. 2008; Schruba et al. 2011). Presenting equation (6) for the molecular and total gas helps to see the way the $\rm M_{HI}$

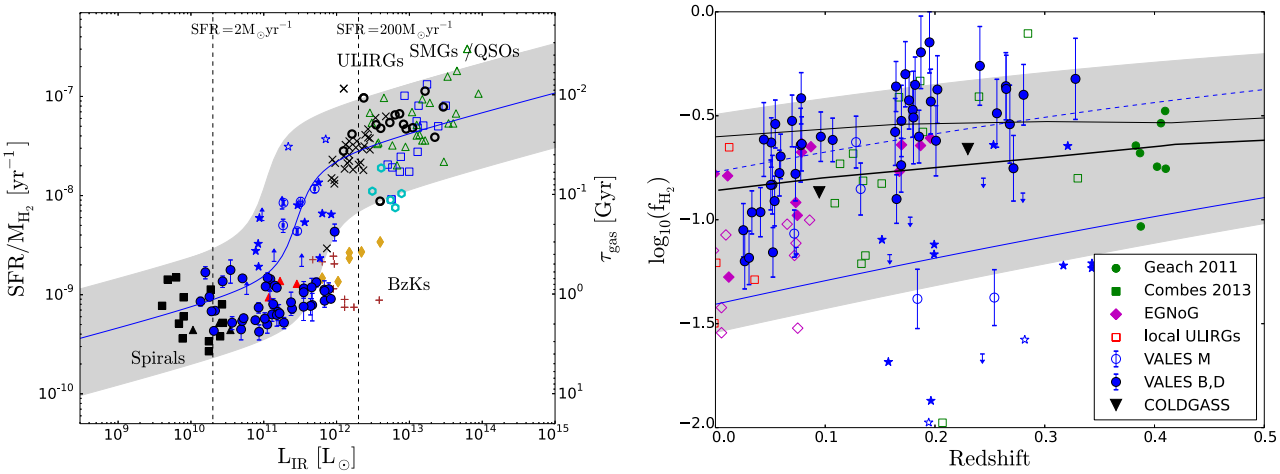

Figure 7. *Left*: SFE versus IR luminosities following the same symbols and colours shown in the left-hand panel of Fig. 5. Blue solid line is the best-fitting parametrization considering all the galaxy samples at $z < 0.4$ presented in the figure (see equation 7) while the light grey area is the region within a 1σ scatter of 0.5 dex. This parametrization suggests a break on the star formation efficiency at $L_{\rm IR} = 10^{11-12}\,{\rm L}_{\odot}$. *Right*: Molecular gas fraction ($f_{M_{\rm H_2}}$) versus redshift for different samples of SFGs. The upside down triangles are the average values from COLDGASS survey. The dashed and solid blue curves are the average behaviour for normal galaxies and the expected location for starburst galaxies by Bauermeister et al. (2013), respectively. The light grey area is the region of the 'main-sequence' for SFGs when adopting an average $\tau_{M_{\rm H_2}}({\rm MS}) \sim 2.2$ Gyr (e.g. Bigiel et al. 2008; Leroy et al. 2008). The two black curves show semi-analytic prescriptions for galaxy formation by Lagos et al. (2011), which correspond to mass halo models of $M_{\rm h} = 10^{11}$ and $10^{12}\,{\rm M}_{\odot}\,{\rm h}^{-1}$, from thinnest to thickest, respectively.

could affect our results. In particular we find that the slope is flatter when $M_{\rm gas}$ are used. We highlight that given that these galaxies have been selected in the far-IR, our results are not significantly affected by the assumptions in geometrical modelling of the dust as previous in Genzel et al. (2013) and Freundlich et al. (2013) studies.

If we take into account the samples of galaxies belonging to the sequence of discs shown in right-hand panel of Fig. 6 (including $z = 1.0$–2.3 normal galaxies, BzK and $z \sim 0.5$ discs, spiral galaxies and both our spatially resolved and unresolved B-/D-dominated galaxies) in our linear regression of equation (6), we obtain a slope of 1.26 ± 0.02 and a normalization of 3.6 ± 0.2. Mentioned before, this should be taken with caution as there is growing evidence for a cosmic evolution of the star formation efficiency, effective radius and gas content (e.g. Magdis et al. 2012), implying that the combination of samples at different epochs might be mixing intrinsically different populations.

3.4 Star formation efficiency

We define the star formation efficiency as ${\rm SFE} = {\rm SFR}/M_{\rm H_2}$ and the $M_{\rm H_2}$ consumption time-scale ($\tau_{M_{\rm H_2}}$) as ${\rm SFE}^{-1}$. In the left-hand panel of Fig. 7, we show the SFE versus $L_{\rm IR}$ for our galaxies including other galaxy samples taken from the literature. Two distinctive types of galaxies are evident: those galaxies that present a long-standing mode of star formation with $\tau_{\rm MH2} \sim 1.3$ Gyr; and those affected by a much faster starburst processes with $\tau_{M_{\rm H_2}} \sim 0.2$ Gyr. We identify a significant number of sources that are located in the 'transition zone' between both the sequence of discs and the sequence of starbursts (left-hand panel in Fig. 7), with SFEs in the range of 4.3–11.7 Gyr^{-1}, and with a median of 8.5 ± 0.1 Gyr^{-1} (e.g. similar to those SMGs at $z = 0.22$–0.25 presented by Ivison et al. 2011). These sources seem to suggest the co-existence of both modes of star formation at intermediate efficiencies. We note that 39 of our sources are located in the long-lasting mode, with SFEs in the range of 0.42–4.32 Gyr^{-1}, and with a median of 0.8 ± 0.1 Gyr^{-1}.

We highlight the evidence for galaxies located in the 'transition zone' between 'normal' and 'starburst' confirming a break in SFE at $L_{\rm IR} \approx 10^{11-12}\,{\rm L}_{\odot}$, which could indicate the possibility of a single evolutionary path (with a large scatter) rather than a sharp bimodal behaviour in evolution (see Section 3.2). This is in agreement with previous findings by Sargent et al. (2014). We propose an empirical best-fitting parametrization to describe the dependence of the SFE on $L_{\rm IR}$ (based in all $z < 0.4$ samples included in left-hand panel of Fig. 7):

$$\log[{\rm SFR}/M_{\rm H_2}\,({\rm yr}^{-1})] = 0.19 \times (\log[L_{\rm IR}/{\rm L}_{\odot}] - \phi) + \alpha + \beta \arctan[\rho\,(\log[L_{\rm IR}/{\rm L}_{\odot}] - \phi)], \quad (7)$$

where $\alpha = -8.26$, $\beta = -0.41$, $\rho = -4.84$ and $\phi = 11.45$. This function has a scatter of $\sigma = 0.5$ dex.

In this work, we highlight that our method to compute the molecular gas masses is directly using CO(1–0), not assuming any particular conversion for high-J transitions, facilitating the interpretation of the results. Scoville et al. (2016), for example, obtain different star formation modes for normal and starburst/SMG galaxies, which are likely affected by the different methods behind the computation of both gas masses at high redshift (using higher J CO transitions) and different $\alpha_{\rm CO}$ for each type of galaxy.

In spite of the remaining uncertainties on the assumptions used to derive $M_{\rm H_2}$, the detection of galaxies in the 'transition zone', including spectrally detected/undetected with $\alpha_{\rm CO} = 4.6\,({\rm K\,km\,s^{-1}\,pc^2})^{-1}$ and mergers with a smaller $\alpha_{\rm CO}$ by a factor of six, supports the scenario of a smooth increase of SFE as a function of $L_{\rm IR}$. This has been hinted before in galaxies at $z = 1.6$ by Silverman et al. (2015), where as they explored sources above the 'main sequence' they tentatively concluded a smooth increase of SFE instead of a bimodality in star formation modes.

3.5 Evolution of the molecular gas fraction

In this section, we explore the evolution of the molecular gas fraction ($f_{\rm H_2}$) as a function of redshift. We introduce the molecular gas mass

to the stellar mass ratio as:

$$\frac{M_{\rm H_2}}{M_\star} = \tau_{\rm M_{H2}} \times {\rm sSFR}, \quad (8)$$

thus, the gas fraction can be calculated as $f_{\rm H_2} = M_{\rm H_2}/(M_{\rm H_2} + M_\star)$. We find our sample covers a wide range of values $f_{\rm H_2} \sim 0.04$–0.71 (for those sources spectrally CO detected above 5σ), which are similar to those shown by the Evolution of molecular Gas in Normal Galaxies (Bauermeister et al. 2013) survey in normal SFGs. Compared to local ULIRGs, where $f_{\rm H_2}$ ranges at 3–5 per cent (e.g. Solomon et al. 1997; Gao & Solomon 2004; Chung et al. 2009), our gas fractions are typically higher than those, although if we only consider those M-dominated galaxies we find similar values to those seen in local ULIRGs (lying near the lower $f_{\rm H_2}$ envelope defined for starburst galaxies by Bauermeister et al. 2013). We identify that our $f_{\rm H_2}$ values show a tendency to increase as a function of redshift (see Fig. 7) – probably product of a selection effect induced by the *Herschel* detectability (these are dusty galaxies). Béthermin et al. (2014) suggest a rapid increase of the average fraction of molecular gas with redshift, similarly to what we find in our analysis. Based on recent works (e.g. Dunne et al. 2011; Hardcastle et al. 2016; Wang et al. 2017), there is growing evidence for a rapid galaxy evolution at low redshifts. Particularly, Dunne et al. (2011) find evidence for fast evolution of the dust mass content of galaxies up to $z = 0.5$, a result that suggest that the molecular gas content also rapidly evolves in samples of *Herschel*-selected galaxies. Actually, using galaxies taken from this same work, Hughes et al. (2017a) suggests that this rapid evolution goes together with a significant increment of the gas density (up to $z = 0.2$), aided by predictions from photodissociation region modelling.

In the right-hand panel of Fig. 7, the two black curves show semi-analytic prescriptions for galaxy formation and evolution of the molecular ISM computed by Lagos et al. (2011), based on an empirical star formation law to estimate the molecular gas mass. Black solid lines correspond to mass halo models of $M_{\rm h} = 10^{11}$ and $10^{12}\,{\rm M_\odot\,h^{-1}}$, from thinnest to thickest, respectively, that trace our B- and D-dominated galaxies. These models suggest that molecular gas mass content and SFR densities increase as a function of redshift, in rough agreement with what we see in our B- and D-dominated galaxies. On the other hand, the M-dominated galaxies are apparently associated to more massive dark matter haloes of $\sim 10^{12}\,{\rm M_\odot}$.

4 CONCLUSIONS

In this paper, we present the VALES survey – one of the largest samples of CO-detected normal SFGs up to $z = 0.35$. We use the ALMA telescope to estimate the molecular gas content via CO(1–0) emission in a sample of 67 dusty SFGs. Sources are bright far-IR emitters ($S_{160\,\mu{\rm m}} \geq 100$ mJy; $L_{\rm IR} \approx 10^{10-12}\,{\rm M_\odot}$) selected from the equatorial fields of the *H*-ATLAS survey (with SFRs in the range of 1.4–94.2 $\rm M_\odot\,yr^{-1}$). We have spectroscopically detected 49 galaxies (72 per cent of the sample) with a $>5\sigma$ CO peak line significance and 12 others are detected in collapsed spectra at low signal to noise. We find that 21 galaxies are spatially resolved in CO (with physical sizes in the range of 3.7–35.1 kpc, allowing a multiwavelength exploration over a wide parameter space. We summarize our main results as follows:

(i) Based on a visual inspection to the optical/near-IR photometry of the 49 spectrally CO-detected galaxies, we classify 36 per cent as being dominated by a (B)ulge morphology, 53 per cent as a (D)isk morphology and 11 per cent show evidence for a (M)erger event or interaction. We spatially resolve 21 galaxies that on average show optical-to-CO size ratios of $\sim 1.6 \pm 0.5$; hence, the molecular gas is more concentrated towards the central regions than the stellar component.

(ii) Our sample explores the $L'_{\rm CO}$ luminosity range of 0.3×10^{10} K km s^{-1} pc^2 expanding the parameter space to fainter values than previous relevant CO surveys at similar redshifts. Aided by the morphological classification (assuming standard $\alpha_{\rm CO}$ conversion factors for discs and mergers), we estimate a range of $M_{\rm H_2} = 10^{8.9-10.9}\,{\rm M_\odot}$ for bulge- and disc-dominated galaxies while $10^{9.3-9.8}\,{\rm M_\odot}$ for merger-dominated galaxies.

(iii) We explore the Schmidt–Kennicutt relation using values for global $\Sigma_{\rm SFR}$ and $\Sigma_{M_{\rm gas}}$ derived from a combination of CO and optical radii. Our sample perfectly complements the parameter space that joins both, local and high-z 'normal' galaxy samples. We find a best linear fit with a power law slope of 1.16 ± 0.05 and 1.27 ± 0.05 when using $M_{\rm H_2}$ and $M_{\rm H_2} + {\rm H\,I}$, respectively.

(iv) The median SFE of our sample is 8.5 Gyr^{-1} (with values in the range of 0.4–11.7 Gyr^{-1}). Even though most of our galaxies follow a long-standing mode of star formation activity, we provide evidence for a population with efficiencies in the 'intermediate valley' between normal star formation in discs and more rapid/violent starburst episodes. Within some galaxies, there may be a mixture of star formation modes occurring at the same time. We propose the existence of a continuous transition for the star formation efficiencies as a function of far-IR luminosities.

(v) We estimate the molecular gas fraction, finding values in the range of $f_{\rm H_2} = 0.06$–0.34. Our observations suggest a strong increment of the gas fraction as a function of redshift (up to $z = 0.35$), faster than semi-analytical models predictions. This rapid evolution might be affected by the selection criteria as we are selecting *Herschel*-detected galaxies with preferentially high dust content.

To conclude, we note that one of the main uncertainties in this work is produced by the different CO conversion factors between CO luminosity and molecular gas mass, which undoubtedly impact our estimates. Two of the most evident drivers of these uncertainties are the dynamical state of the galaxies and the metallicity. We are putting special emphasis on tackling the uncertainty on the molecular gas mass estimates using dynamical modelling of resolved galaxies (Molina et al., in preparation), the physical conditions of the interstellar molecular gas within them (Hughes et al. 2017a) and the calibration between the dust continuum luminosity and interstellar gas content (Hughes et al. 2017b).

ACKNOWLEDGEMENTS

EI and TMH acknowledge CONICYT/ALMA funding Program in Astronomy/PCI Project N°:31140020. MA acknowledges partial support from FONDECYT through grant 1140099. This paper makes use of the following ALMA data: ADS/JAO.ALMA 2012.1.01080.S and ADS/JAO.ALMA 2013.1.00530.S. ALMA is a partnership of ESO (representing its member states), NSF (USA) and NINS (Japan), together with NRC (Canada), NSC and ASIAA (Taiwan), and KASI (Republic of Korea), in cooperation with the Republic of Chile. The Joint ALMA Observatory is operated by ESO, AUI/NRAO and NAOJ. The *Herschel*-ATLAS is a project with *Herschel*, which is an ESA space observatory with science instruments provided by European-led Principal Investigator consortia and with important participation from NASA. The *H*-ATLAS website is http://www.h-atlas.org/. PACS has been developed by

a consortium of institutes led by MPE (Germany) and including UVIE (Austria); KU Leuven, CSL, IMEC (Belgium); CEA, LAM (France); MPIA (Germany); INAF-IFSI/OAA/OAP/OAT, LENS, SISSA (Italy); IAC (Spain). This development has been supported by the funding agencies BMVIT (Austria), ESA-PRODEX (Belgium), CEA/CNES (France), DLR (Germany), ASI/INAF (Italy) and CICYT/MCYT (Spain). SPIRE has been developed by a consortium of institutes led by Cardiff University (UK) and including Univ. Lethbridge (Canada); NAOC (China); CEA, LAM (France); IFSI, Univ. Padua (Italy); IAC (Spain); Stockholm Observatory (Sweden); Imperial College London, RAL, UCL-MSSL, UKATC, Univ. Sussex (UK); and Caltech, JPL, NHSC, Univ. Colorado (USA). This development has been supported by national funding agencies: CSA (Canada); NAOC (China); CEA, CNES, CNRS (France); ASI (Italy); MCINN (Spain); SNSB (Sweden); STFC, UKSA (UK); and NASA (USA). GAMA is a joint European-Australasian project based around a spectroscopic campaign using the Anglo-Australian Telescope. The GAMA input catalogue is based on data taken from the Sloan Digital Sky Survey and the UKIRT Infrared Deep Sky Survey. Complementary imaging of the GAMA regions is being obtained by a number of independent survey programmes including *GALEX* MIS, VST KiDS, VISTA VIKING, WISE, *Herschel*-ATLAS, GMRT and ASKAP providing UV to radio coverage. GAMA is funded by the STFC (UK), the ARC (Australia), the AAO, and the participating institutions. The GAMA website is http://www.gama-survey.org/. DR acknowledges support from the National Science Foundation under grant number AST-1614213 to Cornell University. HD acknowledges financial support from the Spanish Ministry of Economy and Competitiveness (MINECO) under the 2014 Ramn y Cajal program MINECO RYC-2014-15686. LD, SJM and RJI acknowledge support from European Research Council Advanced Investigator Grant COSMICISM, 321302; SJM and LD are also supported by the European Research Council Consolidator Grant COSMICDUST (ERC-2014-CoG-647939, PI H L Gomez).

REFERENCES

Adelman-McCarthy J. K. et al., 2008, ApJS, 175, 297
Aravena M. et al., 2016, MNRAS, 457, 4406
Bauermeister A. et al., 2013, ApJ, 768, 132
Béthermin M. et al., 2014, A&A, 567, A103
Bigiel F., Blitz L., 2012, ApJ, 756, 183
Bigiel F., Leroy A., Walter F., Brinks E., de Blok W. J. G., Madore B., Thornley M. D., 2008, AJ, 136, 2846
Bolatto A. D., Wolfire M., Leroy A. K., 2013, ARA&A, 51, 207
Bolatto A. D. et al., 2015, ApJ, 809, 175
Bothwell M. S., Kennicutt R. C., Lee J. C., 2009, MNRAS, 400, 154
Bothwell M. S. et al., 2013, MNRAS, 429, 3047
Bothwell M. S. et al., 2014, MNRAS, 445, 2599
Bouché N. et al., 2007, ApJ, 671, 303
Bournaud F., Elmegreen B. G., Martig M., 2009, ApJ, 707, L1
Bourne N. et al., 2016, MNRAS, 462, 1714
Braun R., Popping A., Brooks K., Combes F., 2011, MNRAS, 416, 2600
Chabrier G., 2003, ApJ, 586, L133
Chung A., Narayanan G., Yun M. S., Heyer M., Erickson N. R., 2009, AJ, 138, 858
Combes F., García-Burillo S., Braine J., Schinnerer E., Walter F., Colina L., 2011, A&A, 528, A124
Combes F., García-Burillo S., Braine J., Schinnerer E., Walter F., Colina L., 2013, A&A, 550, A41
Combes F., the PHIBSS collaboration 2016, Proc. IAUSymp. 315, From Interstellar Clouds to Star-Forming Galaxies: Universal Processes? Cambridge Univ. Press, Cambridge, p. 240
Crain R. A. et al., 2015, MNRAS, 450, 1937
da Cunha E., Charlot S., Elbaz D., 2008, MNRAS, 388, 1595
Di Matteo P., Combes F., Melchior A.-L., Semelin B., 2007, A&A, 468, 61
Daddi E. et al., 2009a, ApJ, 694, 1517
Daddi E., Dannerbauer H., Krips M., Walter F., Dickinson M., Elbaz D., Morrison G. E., 2009b, ApJ, 695, L176
Daddi E. et al., 2010a, ApJ, 713, 686
Daddi E. et al., 2010b, ApJ, 714, L118
Dekel A., Sari R., Ceverino D., 2009, ApJ, 703, 785
Downes D., Solomon P. M., 1998a, ApJ, 507, 615
Downes D., Solomon P. M., 1998b, ApJ, 507, 615
Driver S. P. et al., 2016, MNRAS, 455, 3911
Dunne L. et al., 2011, MNRAS, 417, 1510
Eales S. et al., 2010, PASP, 122, 499
Elbaz D. et al., 2011, A&A, 533, A119
Feldmann R., Hernandez J., Gnedin N. Y., 2012, ApJ, 761, 167
Frayer D. T. et al., 2008, ApJ, 680, L21
Freundlich J. et al., 2013, A&A, 553, A130
Gao Y., Solomon P. M., 2004, ApJ, 606, 271
Geach J. E., Smail I., Moran S. M., MacArthur L. A., Lagos C. d. P., Edge A. C., 2011, ApJ, 730, L19
Genzel R. et al., 2010, MNRAS, 407, 2091
Genzel R. et al., 2012, ApJ, 746, 69
Genzel R. et al., 2013, ApJ, 773, 68
Genzel R. et al., 2015, ApJ, 800, 20
Graciá-Carpio J. et al., 2011, ApJ, 728, L7
Greve T. R. et al., 2005, MNRAS, 359, 1165
Hardcastle M. J. et al., 2016, MNRAS, 462, 1910
Hildebrand R. H., 1983, QJRAS, 24, 267
Houghton S., Whiteoak J. B., Koribalski B., Booth R., Wiklind T., Wielebinski R., 1997, A&A, 325, 923
Howell J. H. et al., 2010, ApJ, 715, 572
Hughes T. M. et al., 2017a, A&A, 602, A49
Hughes T. M. et al., 2017b, MNRAS, preprint (arXiv:1702.07350)
Ibar E. et al., 2013, MNRAS, 434, 3218
Ibar E. et al., 2015, MNRAS, 449, 2498
Ivison R. J., Papadopoulos P. P., Smail I., Greve T. R., Thomson A. P., Xilouris E. M., Chapman S. C., 2011, MNRAS, 412, 1913
Kaneda H., Yamagishi M., Suzuki T., Onaka T., 2009, ApJ, 698, L125
Kennicutt R. C., Jr, 1998, ARA&A, 36, 189
Kennicutt R. C., Evans N. J., 2012, ARA&A, 50, 531
Kennicutt R. C., Jr, Lee J. C., Funes J. G. J. S., Sakai S., Akiyama S., 2008, ApJS, 178, 247
Kennicutt R. C., Jr, et al., 2009, ApJ, 703, 1672
Krumholz M. R., McKee C. F., Tumlinson J., 2009, ApJ, 693, 216
Lagos C. D. P., Lacey C. G., Baugh C. M., Bower R. G., Benson A. J., 2011, MNRAS, 416, 1566
Leroy A. K., Walter F., Brinks E., Bigiel F., de Blok W. J. G., Madore B., Thornley M. D., 2008, AJ, 136, 2782
Leroy A. K. et al., 2009, AJ, 137, 4670
Liske J. et al., 2015, MNRAS, 452, 2087
Magdis G. E. et al., 2012, ApJ, 758, L9
Magdis G. E. et al., 2014, ApJ, 796, 63
Magnelli B. et al., 2012, A&A, 548, A22
Narayanan D., Krumholz M. R., Ostriker E. C., Hernquist L., 2012, MNRAS, 421, 3127
Papadopoulos P. P., Seaquist E. R., 1999, ApJ, 516, 114
Pilbratt G. L. et al., 2010, A&A, 518, L1
Regan M. W., Thornley M. D., Helfer T. T., Sheth K., Wong T., Vogel S. N., Blitz L., Bock D. C.-J., 2001, ApJ, 561, 218
Riechers D. A. et al., 2006, ApJ, 650, 604
Rowlands K. et al., 2014, MNRAS, 441, 1017
Saintonge A. et al., 2011, MNRAS, 415, 32
Salmi F., Daddi E., Elbaz D., Sargent M. T., Dickinson M., Renzini A., Bethermin M., Le Borgne D., 2012, ApJ, 754, L14
Sandstrom K. M. et al., 2013, ApJ, 777, 5
Santini P. et al., 2014, A&A, 562, A30
Sargent M. T. et al., 2014, ApJ, 793, 19

Schaye J. et al., 2015, MNRAS, 446, 521
Schmidt M., 1959, ApJ, 129, 243
Schruba A. et al., 2011, AJ, 142, 37
Scoville N. et al., 2016, ApJ, 820, 83
Shimasaku K. et al., 2001, AJ, 122, 1238
Silverman J. D. et al., 2015, ApJ, 812, L23
Simpson J. M. et al., 2015, ApJ, 807, 128
Smith D. J. B. et al., 2011, MNRAS, 416, 857
Solomon P. M., Vanden Bout P. A., 2005, ARA&A, 43, 677
Solomon P. M., Downes D., Radford S. J. E., Barrett J. W., 1997, ApJ, 478, 144
Spergel D. N. et al., 2003, ApJS, 148, 175
Spergel D. N. et al., 2007, ApJS, 170, 377
Sternberg A., Le Petit F., Roueff E., Le Bourlot J., 2014, ApJ, 790, 10
Tacconi L. J. et al., 2006, ApJ, 640, 228
Tacconi L. J. et al., 2008, ApJ, 680, 246
Tacconi L. J. et al., 2010, Nature, 463, 781
Tacconi L. J. et al., 2013, ApJ, 768, 74
Valiante E. et al., 2016, MNRAS, 462, 3146
Vogelsberger M. et al., 2014, MNRAS, 444, 1518
Wang T. et al., 2017, A&A, 601, A63
Weiß A., Neininger N., Henkel C., Stutzki J., Klein U., 2001, ApJ, 554, L143
Whitaker K. E., van Dokkum P. G., Brammer G., Franx M., 2012, ApJ, 754, L29
Wilson C. D. et al., 2009, ApJ, 693, 1736
Wolfire M. G., Hollenbach D., McKee C. F., 2010, ApJ, 716, 1191
Young J. S. et al., 1995, ApJS, 98, 219
Zhang W., Li C., Kauffmann G., Zou H., Catinella B., Shen S., Guo Q., Chang R., 2009, MNRAS, 397, 1243

APPENDIX

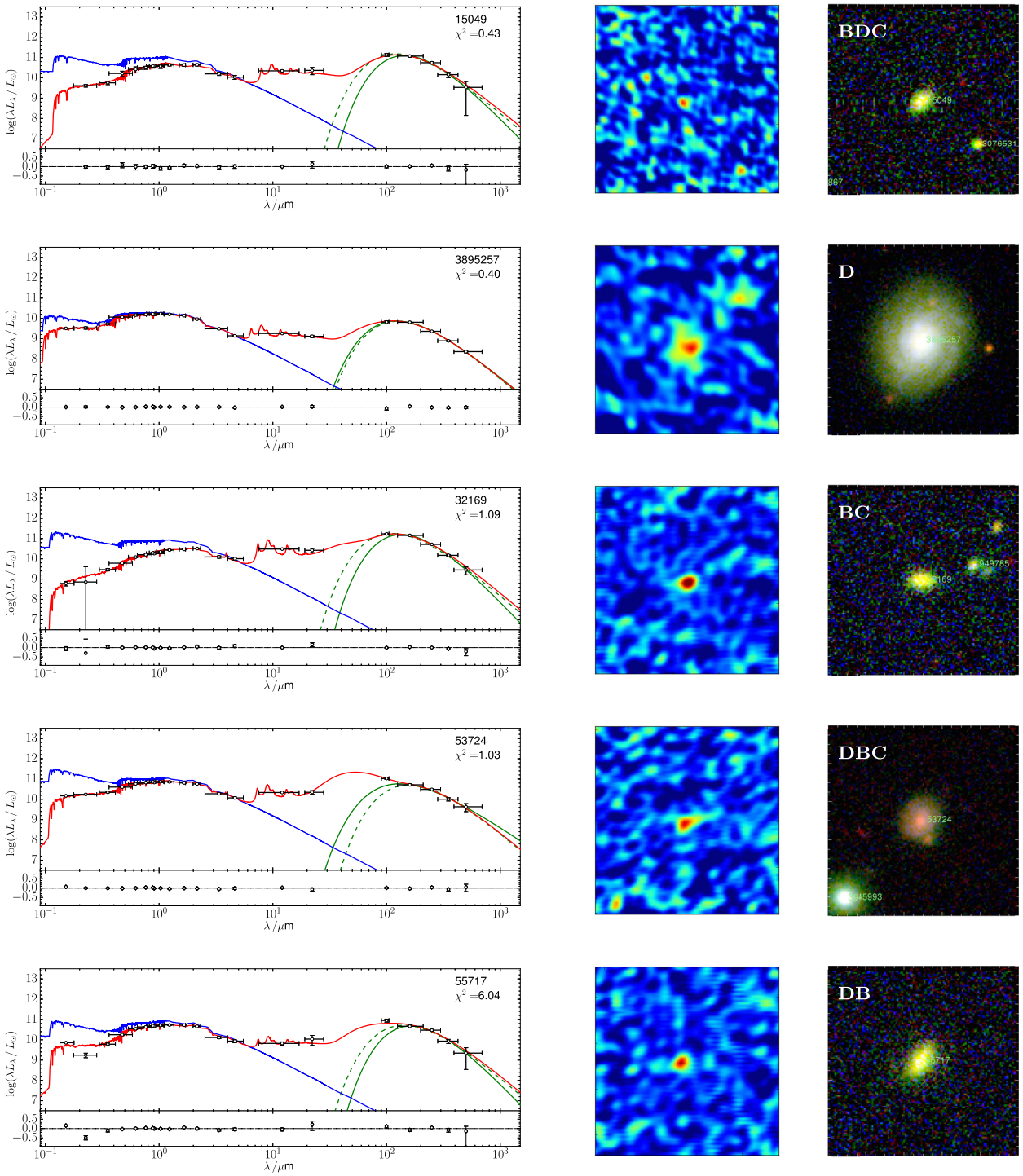

Figure A1. *Left*: Panels show the observed far-UV to submm SED for detected galaxies, constructed from GAMA/*H*-ATLAS photometry (black circles). We model the complete FUV–submm SED using MAGPHYS (da Cunha et al. 2008) to obtain the best-fitting SED (red line) and the unattenuated SED (blue line). We also model the cold dust SED component between 100 and 500 μm by fitting a Hildebrand (1983) one-component modified blackbody model adopting either a fixed emissivity index of $\beta = 1.8$ (green dashed line) or β varying as a free parameter (green solid line). Panels are the residuals between the observed and best-fitting SED model template. Each individual plot is labelled with the GAMA ID of the target and the χ^2 values corresponding to the best-fitting SED template. *Middle*: The collapsed CO cubes. Each panel is 40 arcsec × 40 arcsec in size and centred on the source coordinates. *Right*: Multiband images composed by VISTA *K*-band (red), SDSS *r*-band (green) and SDSS *u*-band (blue) with same size as middle panels. Green numbers are the GAMA ID for the objects present in the field of view.

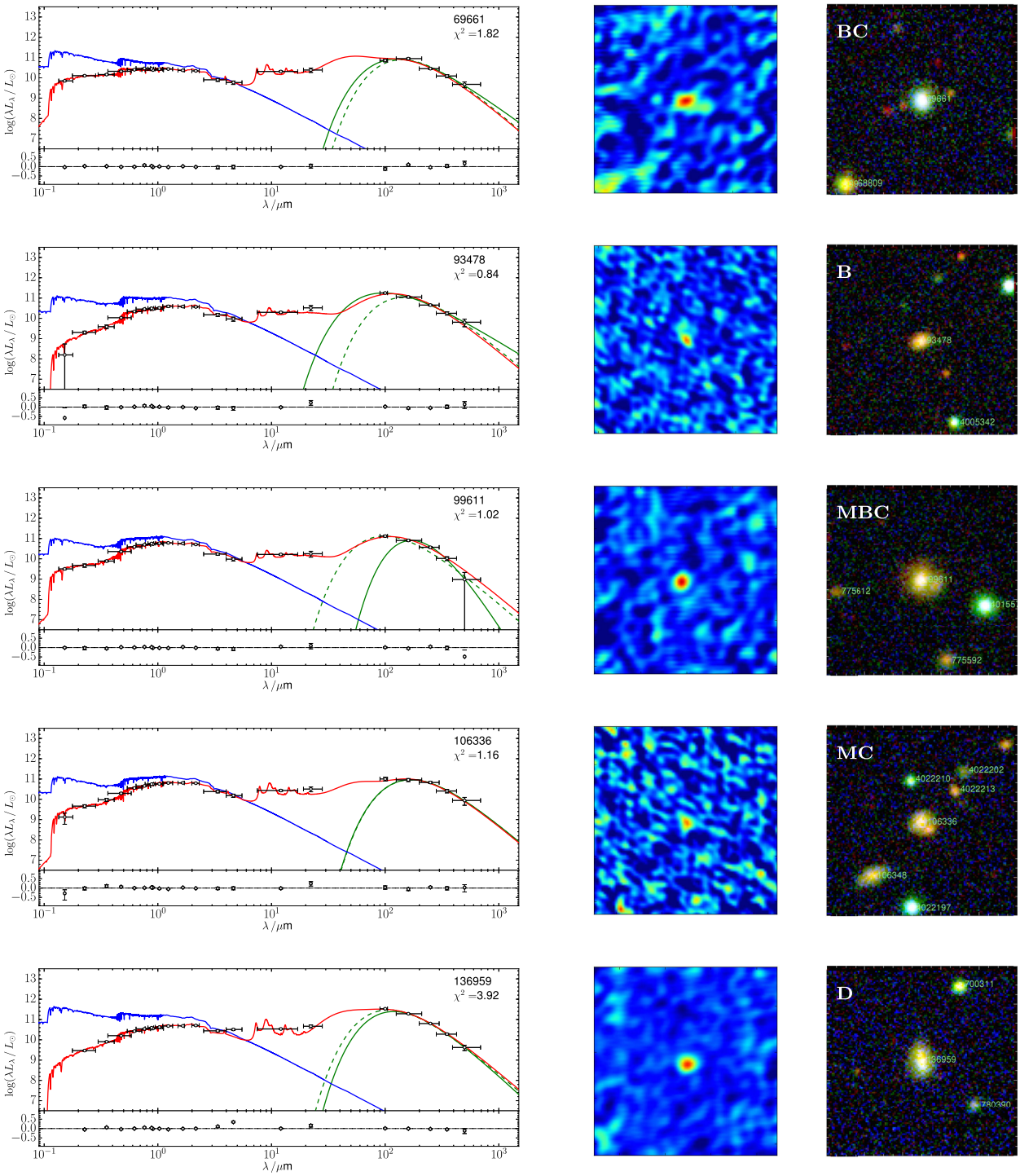

Figure A1 *continued*

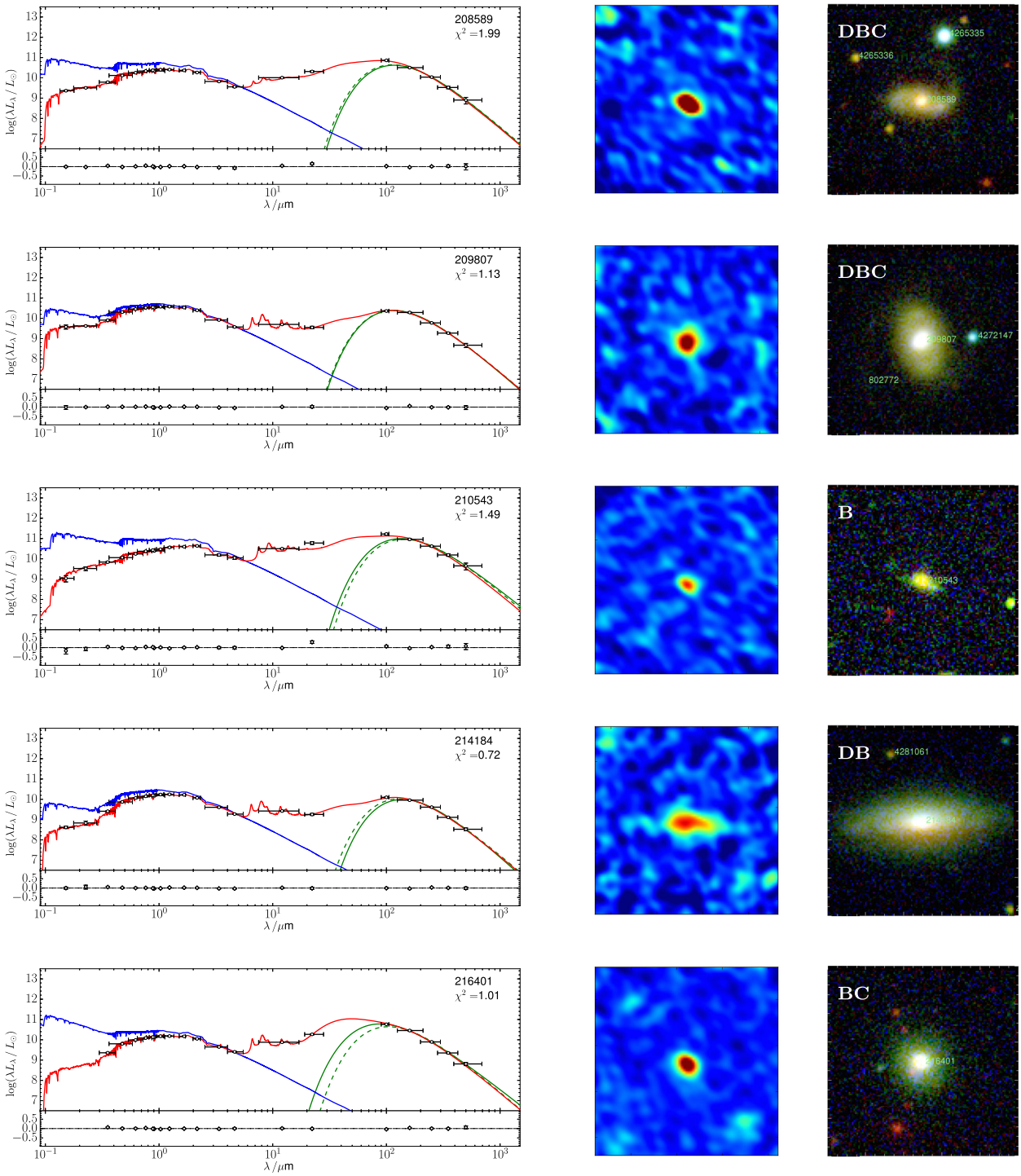

Figure A1 *continued*

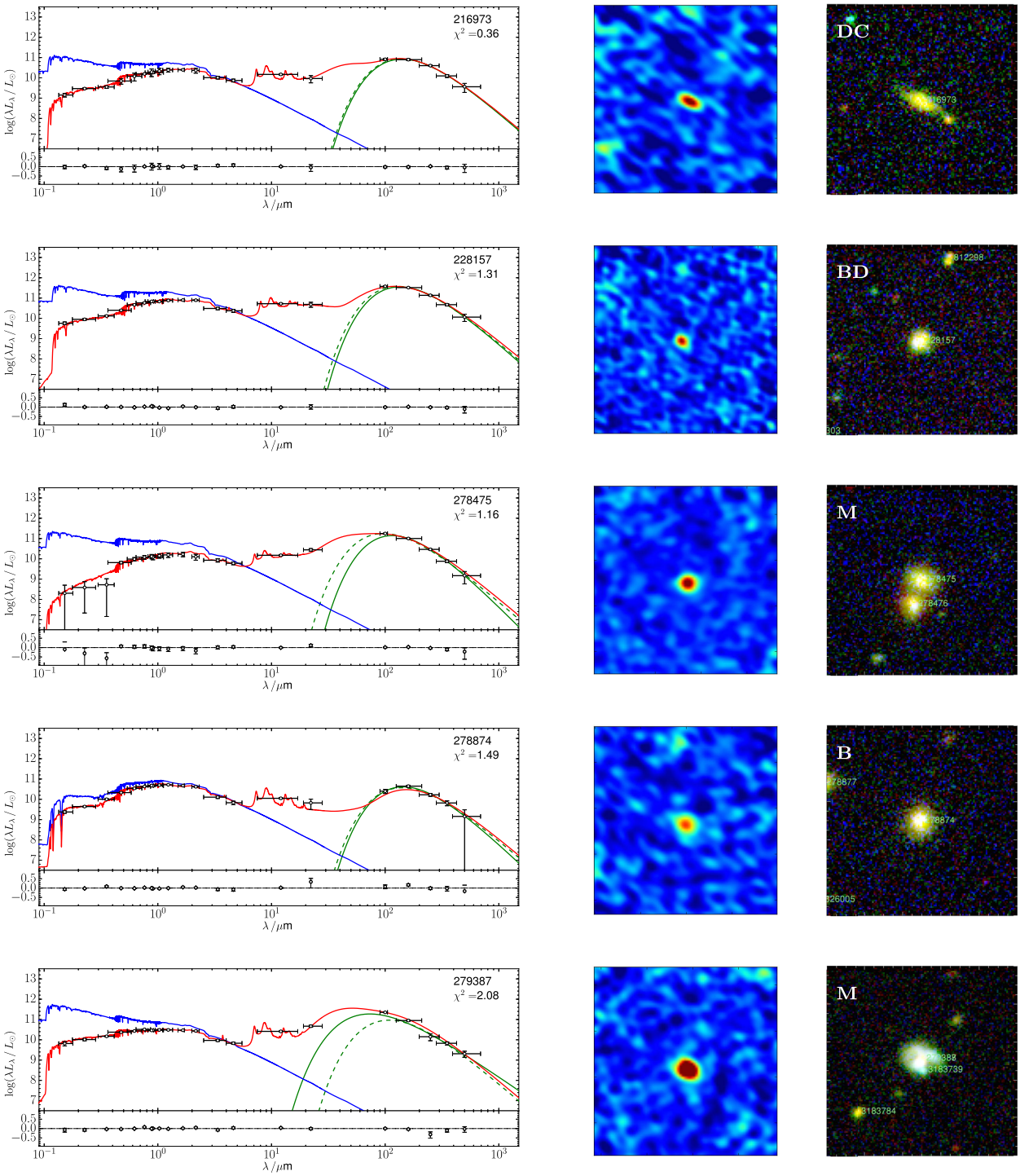

Figure A1 *continued*

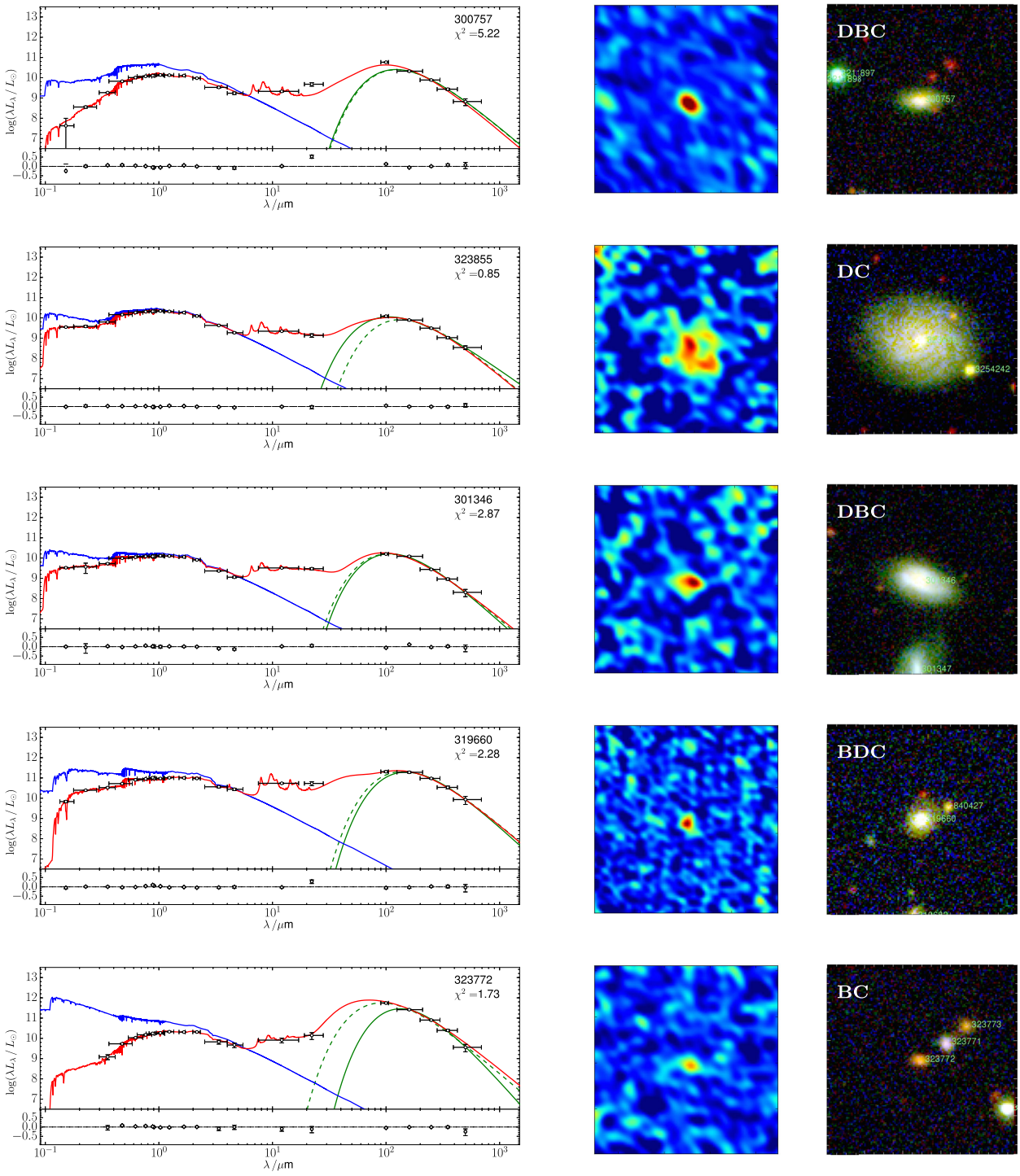

Figure A1 *continued*

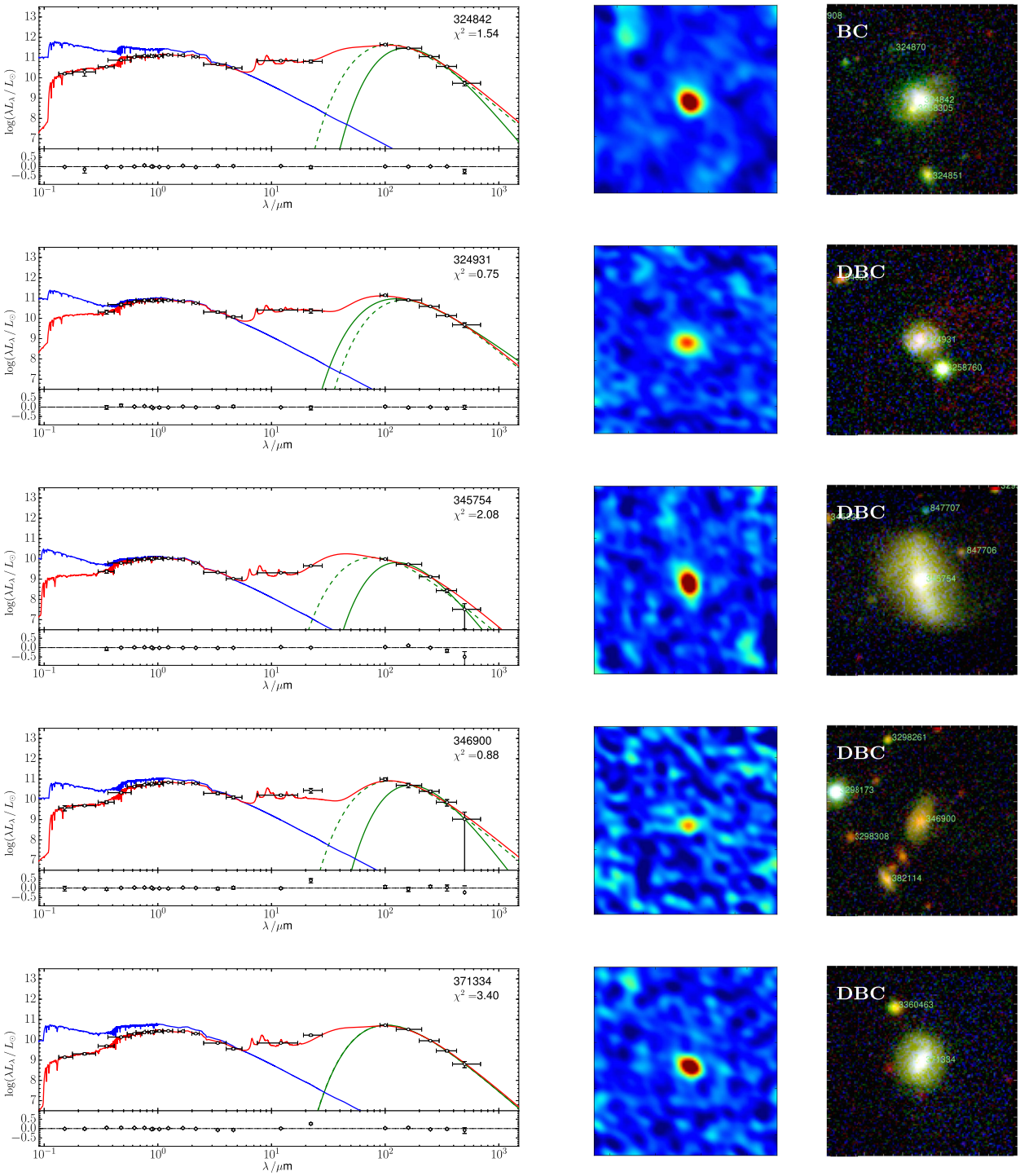

Figure A1 *continued*

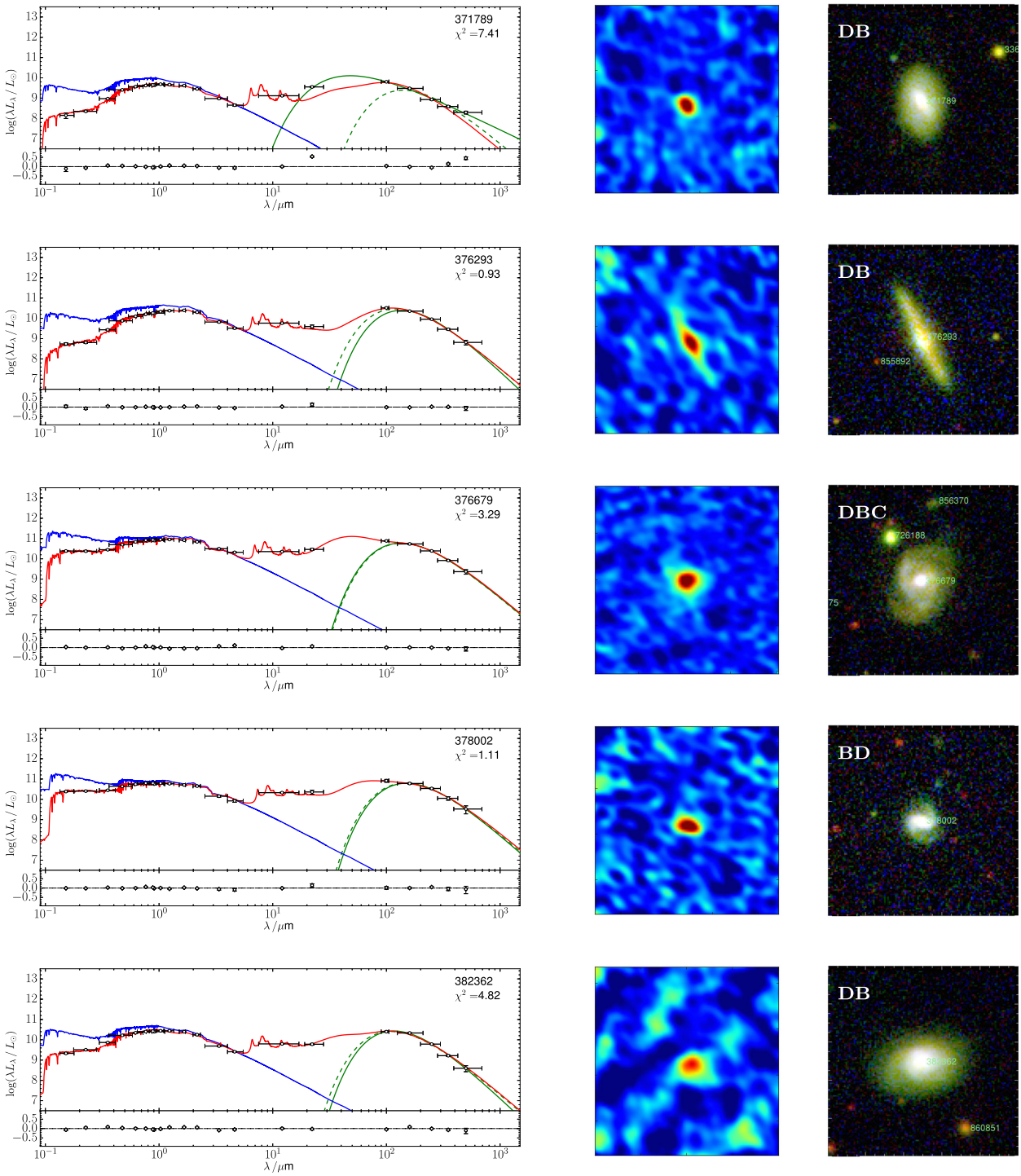

Figure A1 *continued*

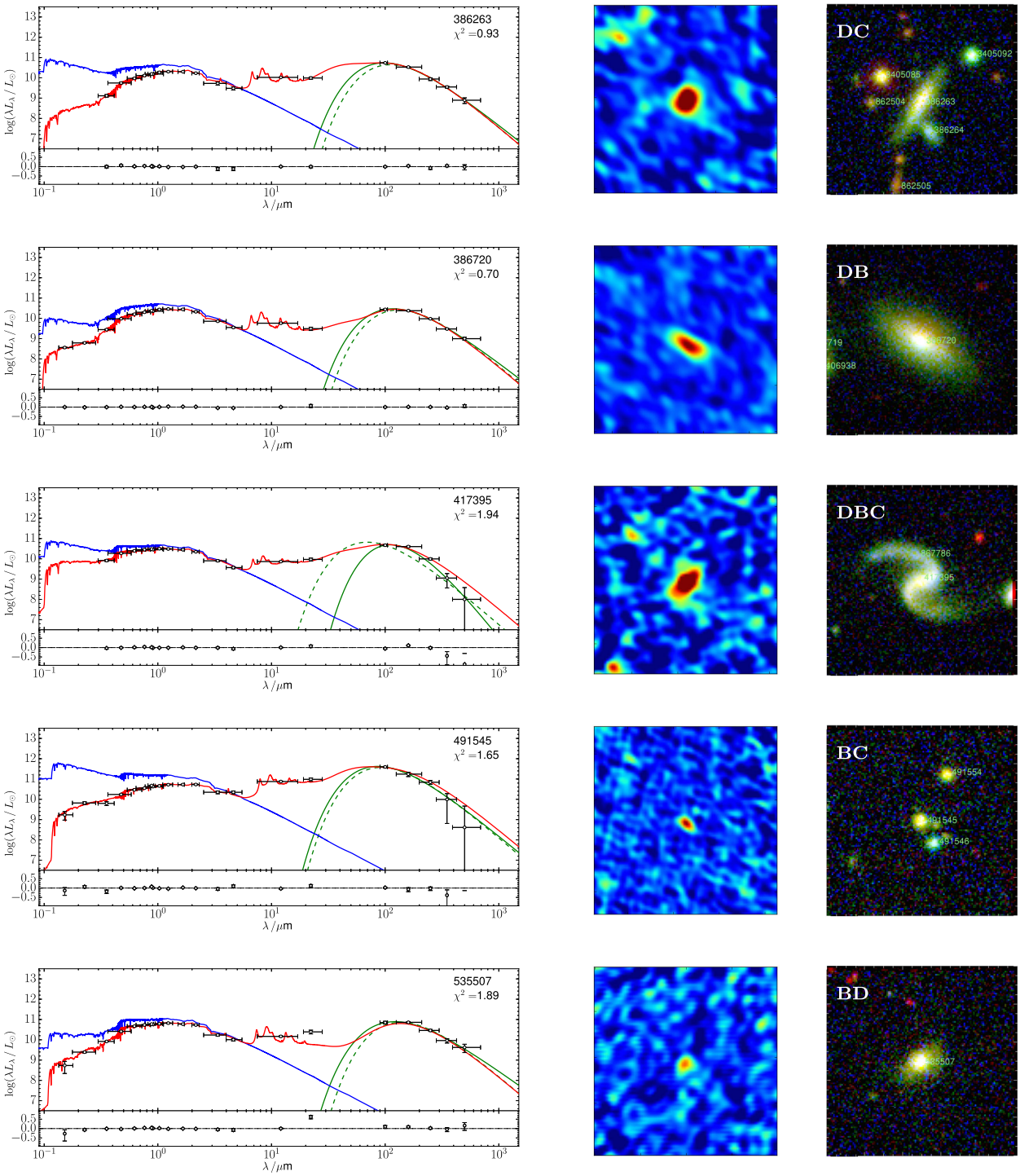

Figure A1 *continued*

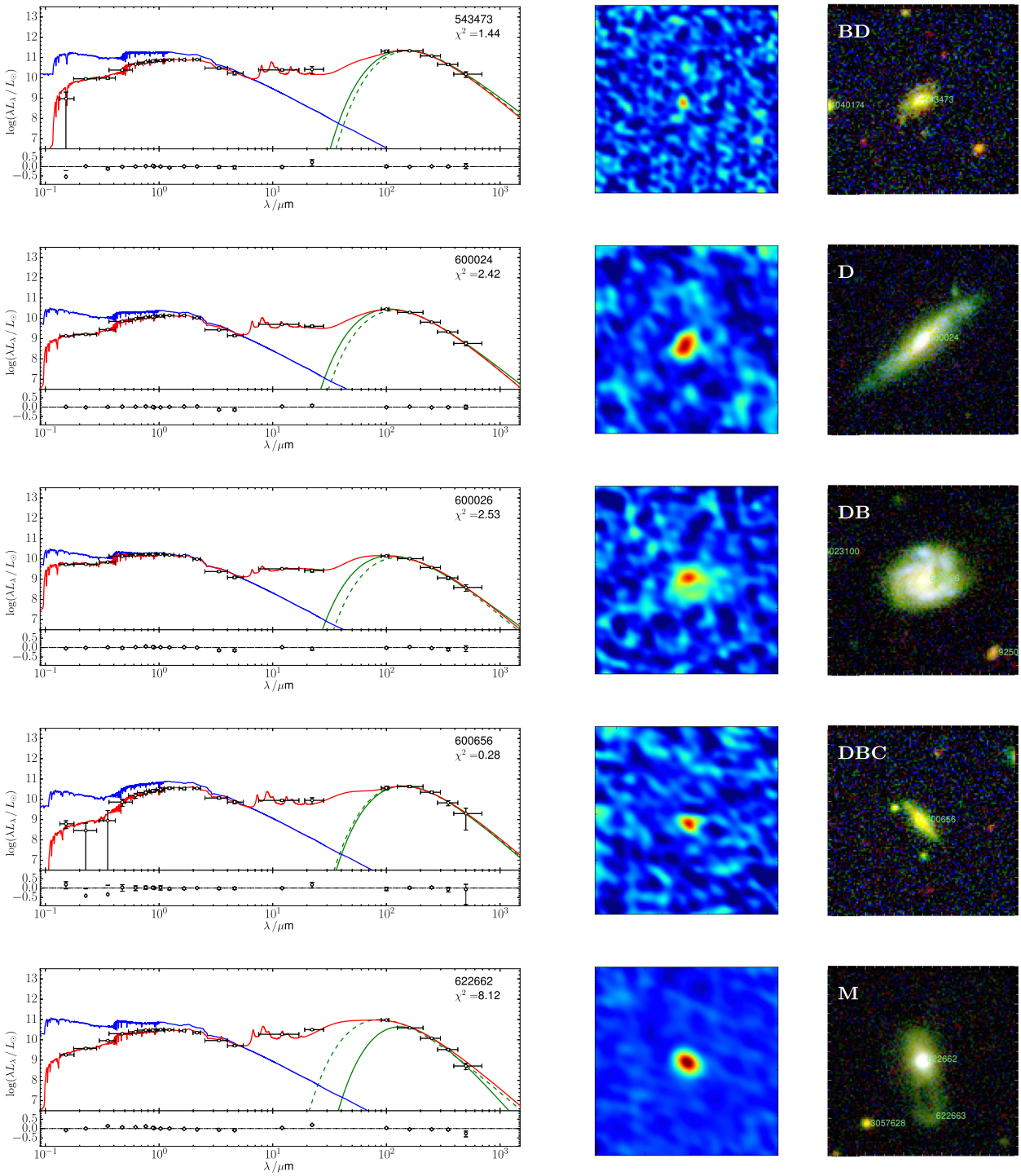

Figure A1 *continued*

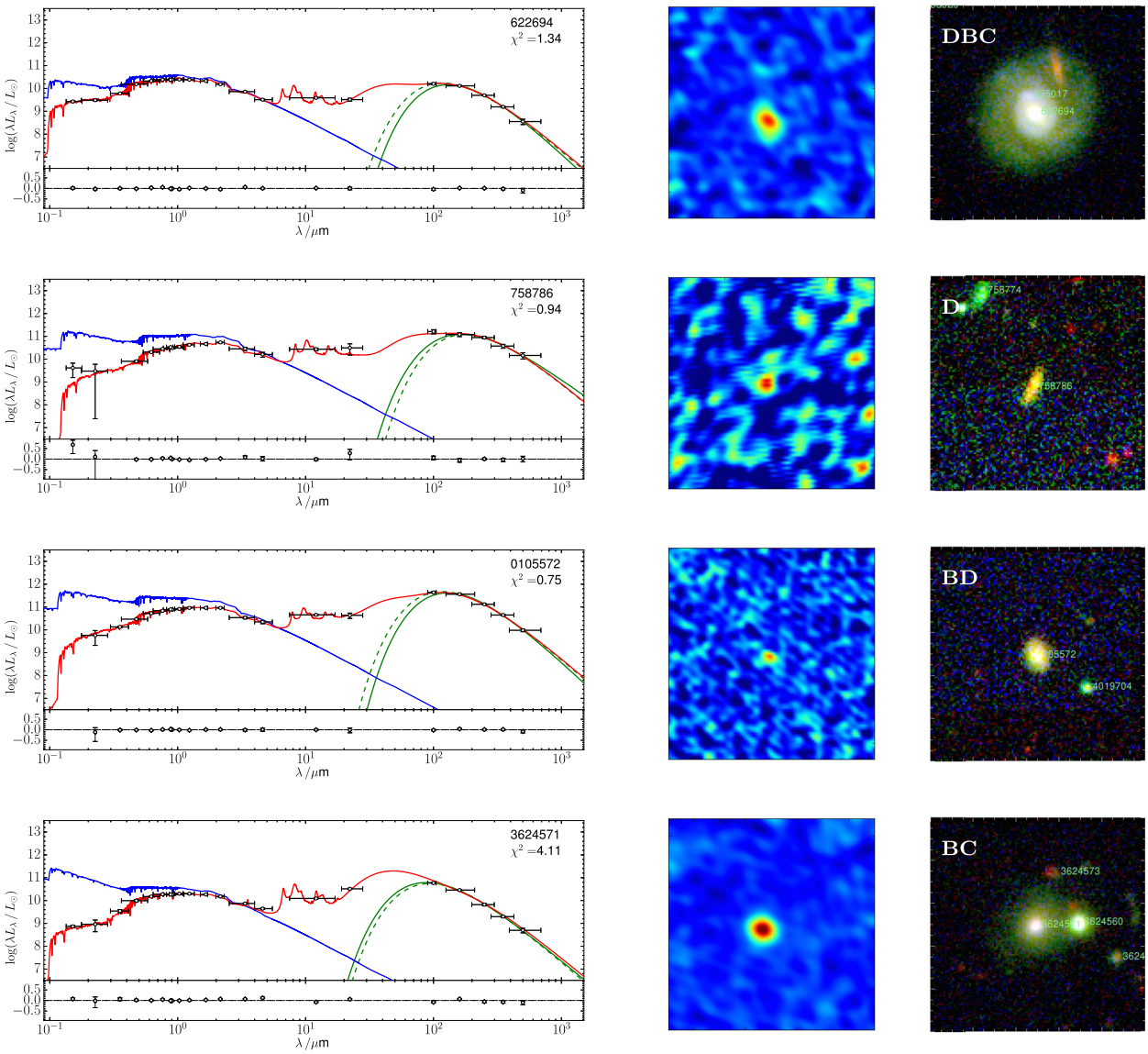

Figure A1 *continued*

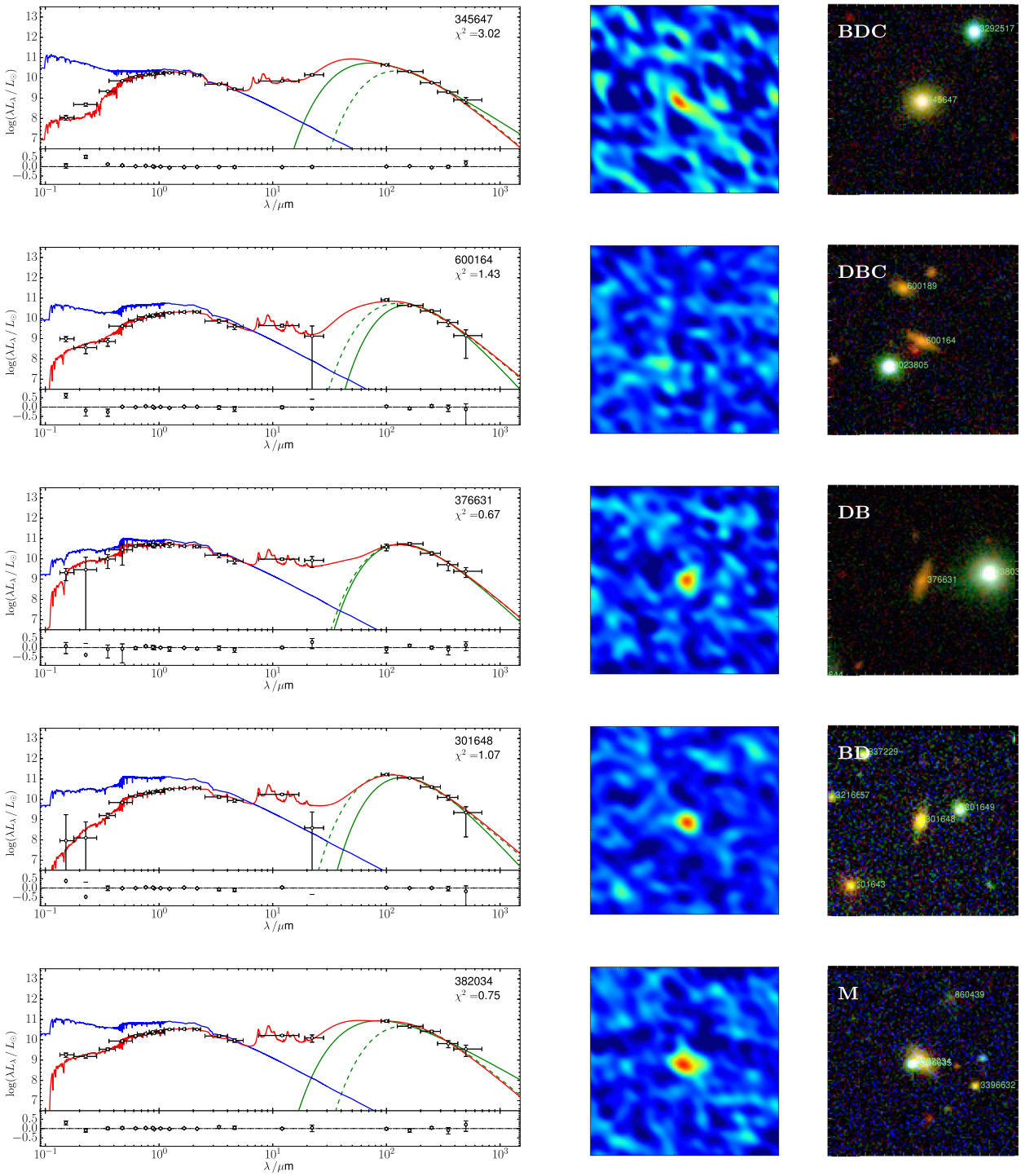

Figure A2. Same as Fig. A1 but for spectrally undetected sources. In these cases the CO cubes are collapsed blindly, between ±250 km s^{-1} from expected observed frequency.

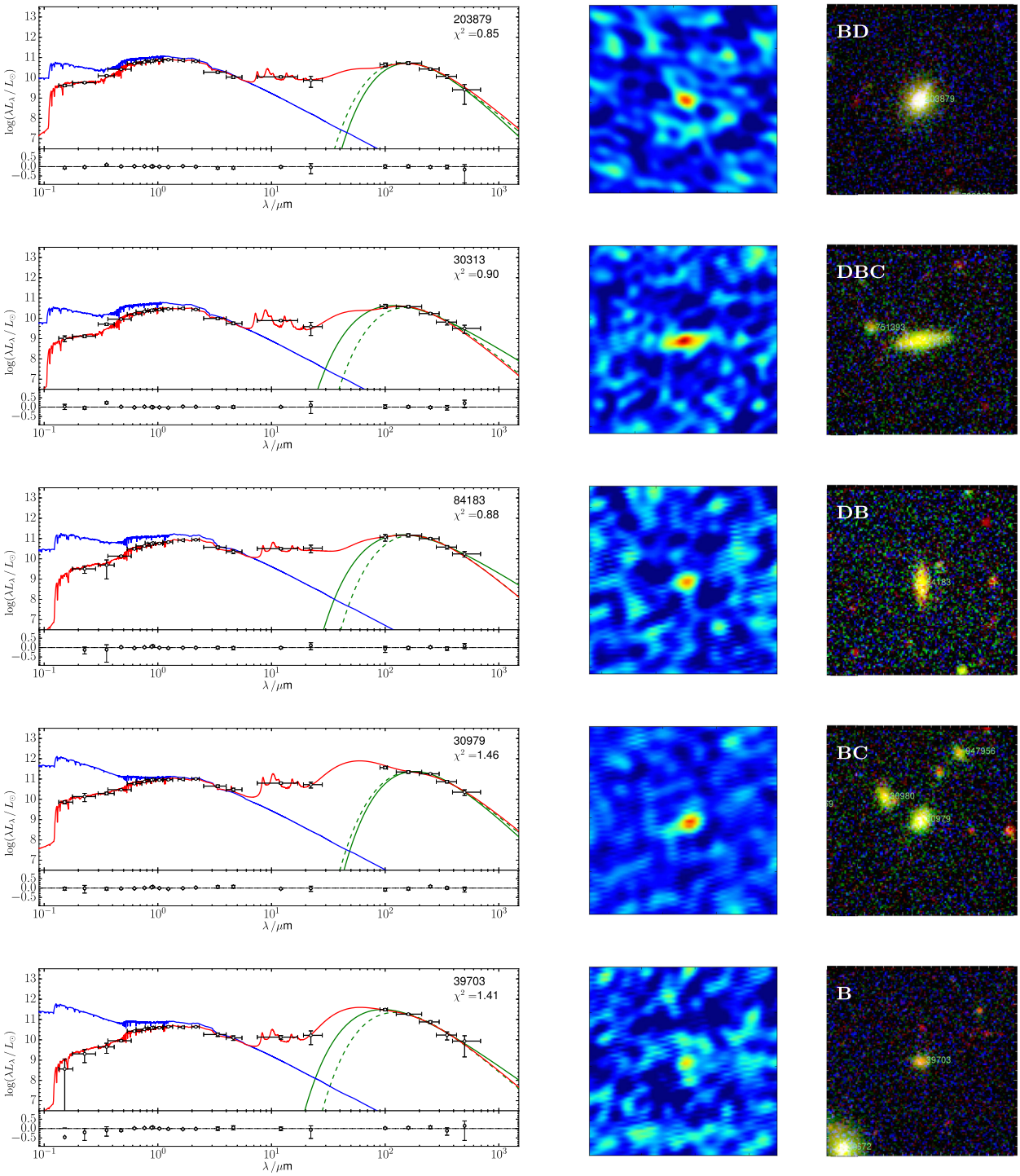

Figure A2 *continued*

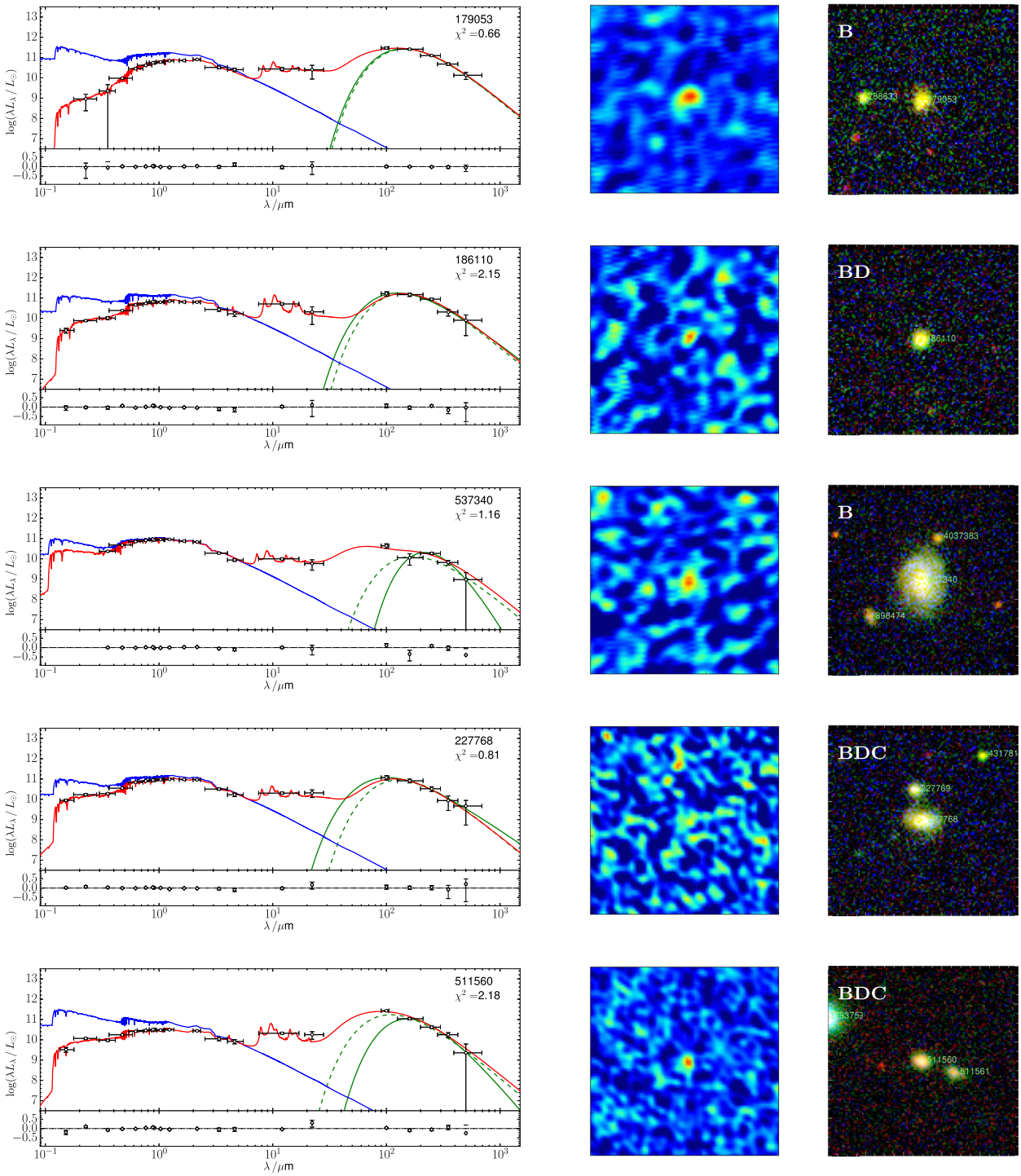

Figure A2 *continued*

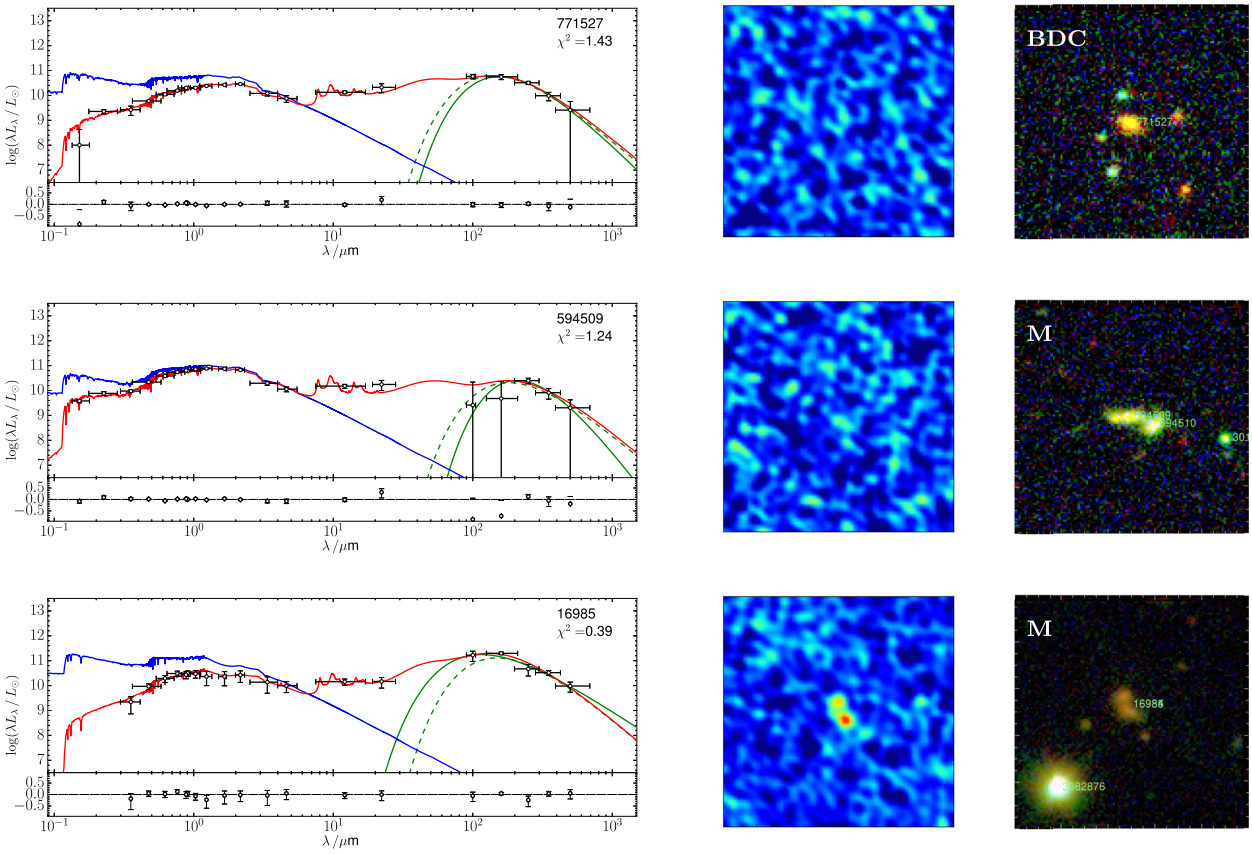

Figure A2 *continued*

[1]*Instituto de Física y Astronomía, Universidad de Valparaíso, Avda. Gran Bretaña 1111, 2340000 Valparaíso, Chile*
[2]*Instituto de Astronomía, Universidad Nacional Autónoma de México, A.P. 70-264, 04510 México, D.F., México*
[3]*Australian Astronomical Observatory, PO Box 915, North Ryde, NSW 1670, Australia*
[4]*Institute for Astronomy, University of Edinburgh, Royal Observatory, Blackford Hill, Edinburgh EH9 3HJ, UK*
[5]*School of Physics and Astronomy, Cardiff University, Queens Buildings, The Parade, Cardiff CF24 3AA, UK*
[6]*European Southern Observatory, Karl-Schwarzschild-Straße 2, D-85748 Garching bei München, Germany*
[7]*Núcleo de Astronomía, Facultad de Ingeniería, Universidad Diego Portales, Av. Ejército 441, 8320000 Santiago, Chile*
[8]*Sterrenkundig Observatorium, Universiteit Gent, Krijgslaan 281 S9, B-9000 Gent, Belgium*
[9]*Department of Physics and Astronomy, University of California, Irvine, CA 92697, USA*
[10]*California Institute of Technology, 1200 E. California Blvd., Pasadena, CA 91125, USA*
[11]*Dpto. Astrofísica, Universidad de La Laguna, E-38206 La Laguna, Tenerife, Spain*
[12]*Instituto de Astrofísica de Canarias (IAC), E-38205 La Laguna, Tenerife, Spain*
[13]*International Centre for Radio Astronomy Research (ICRAR), The University of Western Australia, M468, 35 Stirling Highway, Crawley, WA 6009, Australia*
[14]*School of Physics and Astronomy, University of Nottingham, Nottingham NG7 2RD, UK*
[15]*CAPES Foundation, Ministry of Education of Brazil, 70040-020 Brasilia/DF, Brazil*
[16]*Max-Planck-Institut für Extraterrestrische Physik (MPE), Postfach 1312, D-85741 Garching, Germany*
[17]*Departamento de Astronomía, Universidad de Chile, Casilla 36-D, Santiago, Chile*
[18]*Department of Astronomy, Cornell University, 220 Space Sciences Building, Ithaca, NY 14853, USA*
[19]*Jeremiah Horrocks Institute, University of Central Lancashire, Preston PR1 2HE, UK*
[20]*Dipartimento di Astronomia, Università di Padova, vicolo Osservatorio, 3, I-35122 Padova, Italy*
[21]*Leiden Observatory, Leiden University, PO Box 9513, NL-2300 RA Leiden, the Netherlands*

This paper has been typeset from a TEX/LATEX file prepared by the author.